JM PAPERS

Instabilities in collapsible channel flow with a pre-tensioned elastic beam

Danyang Wang[1,2] ⓘ **, Xiaoyu Luo**[2,†] ⓘ **, Zishun Liu**[3] **and Peter S. Stewart**[2] ⓘ

[1]International Center for Applied Mechanics, State Key Laboratory for Strength and Vibration of Mechanical Structures, School of Aerospace Engineering, Xi'an Jiaotong University, Xi'an 710049, PR China

[2]School of Mathematics and Statistics, University of Glasgow, University Place, Glasgow G12 8QQ, UK

[3]City University of Hong Kong (Dongguan), Dongguan 523808, PR China

Corresponding author: Peter S. Stewart, peter.stewart@glasgow.ac.uk

Hydrodynamic instability can occur when a viscous fluid is driven rapidly through a flexible-walled channel, including a multiplicity of steady states and distinct families of self-excited oscillations. In this study we use a computational method to predict the stability of flow through a planar finite-length rigid channel with a segment of one wall replaced by a thin pre-tensioned elastic beam of negligible mass. For large external pressures, this system exhibits a collapsed steady state that is unstable to low-frequency self-excited oscillations, where the criticality conditions are well approximated by a long-wavelength one-dimensional (1-D) model. This oscillation growing from a collapsed state exhibits a reduced inlet driving pressure compared with the corresponding steady flow, so the oscillating state is energetically more favourable. In some parameter regimes this collapsed steady state is also unstable to distinct high-frequency normal modes, again predicted by the 1-D model. Conversely, for lower external pressures, the system exhibits an inflated steady state that is unstable to another two modes of self-excited oscillation, neither of which are predicted by the lower-order model. One of these modes becomes unstable close to the transition between the upper and lower steady states, while the other involves small-amplitude oscillations about a highly inflated wall profile with large recirculation vortices within the cavity. These oscillatory modes growing from an inflated steady state exhibit a net increase in driving pressure compared with the steady flow, suggesting a different mechanism of instability to those growing from a collapsed state.

Key words: flow-structure interactions, flow-vessel interactions

---

1024 A58-1

1. Introduction

Flow driven rapidly through a flexible-walled tube or channel can exhibit a number of interesting hydrodynamic instabilities that arise through interaction between the flowing fluid and the deformable wall. Such instabilities occur in a number of physiological applications, including fluid flows through compliant conduits in the human body such as the cardiovascular system, the lung airways, the intestinal system and the vocal tract. One striking example of such a physiological instability occurs during syphygmamometry, where blood flow through the compressed brachial artery can exhibit spontaneous self-excited oscillations as the external pressurisation is gradually released, which then manifest as an audible Korotkoff noise. The origins and nonlinear dynamics of such fluid–structure instabilities have been thoroughly reviewed elsewhere, both in the physiological context (e.g. Heil & Hazel 2011; Grotberg 2021) and more widely (e.g. Riley, Gad-el Hak & Metcalfe 1988; Paidoussis 2013).

Such self-excited oscillations are also evident in bench-top experiments involving liquid flow driven through a segment of externally pressurised flexible tubing – a Starling resistor; in some cases these oscillations settle into periodic limit cycles that can be categorised into distinct frequency bands (Bertram, Raymond & Pedley 1990), while in others the dynamics appear chaotic (Bertram, Raymond & Pedley 1991). More recent experiments have extended the analysis using particle image velocimetry methods to visualise the oscillating flow field (Chowdhury & Zhang 2024). Similar experiments have been used to study transition to turbulence in long flexible-walled tubes cast from a polymeric gel, elucidating significant differences in the transition process compared with rigid tubes, including the presence of self-excited oscillations (Verma & Kumaran 2012).

Theoretical study of the mechanisms driving these self-excited oscillations is challenging since one must solve the three-dimensional flow equations coupled to the corresponding motion of the flexible wall. For this reason, fully three-dimensional predictions of the onset of self-excited oscillations and their corresponding limit cycles has been restricted to a very small number of studies (Heil & Boyle 2010; Whittaker *et al.* 2010; Whittaker 2015), with some additional focus on steady flows (Hazel & Heil 2003; Marzo, Luo & Bertram 2005; Zhang, Luo & Cai 2018). Although progress has been made with lower-order (semi-empirical) models of these collapsible tube flows (e.g. Bertram & Pedley 1982; Jensen 1990; Armitstead, Bertram & Jensen 1996), the underlying mechanisms that lead to oscillations are still not fully understood.

Given the difficulty of solving three-dimensional models, a simpler approach to understand the onset of these self-excited oscillations is to consider an analogous system involving flow through a flexible-walled channel. Such systems are typically assumed to be entirely planar and readily predict oscillatory instabilities under a variety of set-ups and flow conditions (e.g. Luo & Pedley 1996; Huang 2001; Jensen & Heil 2003; Heil 2004; Stewart *et al.* 2010; Liu, Luo & Cai 2012). However, such planar set-ups are difficult to realise experimentally (Ikeda *et al.* 1998), and so experiments involving flow through a flexible-walled channel (with significant out-of-plane deformation) have instead focused on transition to turbulence or the enhancement of mixing rather than the onset of self-excited oscillations (e.g. Verma & Kumaramn 2013; Wang & Christov 2022).

In this study we focus entirely on a planar set-up involving flow through a finite-length collapsible channel, which is often used as a prototypical system for testing new numerical methods for studying fluid–structure interaction (e.g. Tang *et al.* 2015; Huang *et al.* 2022). Our focus is instead on obtaining mechanistic insight into the various modes of oscillatory instability that can arise in such set-ups. Within this framework, most theoretical studies have focused on asymmetric arrangements where only a finite-length segment of one wall

of a rigid channel is replaced by a compliant surface (in a set-up introduced by Pedley 1992). However, some recent attention has also focused on two-sided collapsible channels with two compliant panels, where symmetry breaking leads to chaotic motion (Huang *et al.* 2021, 2022).

In this study we revisit the asymmetric arrangement of Pedley (1992), where it has previously been shown that self-excited oscillations can occur in a system driven by either a fixed upstream flow rate (Luo & Pedley 1996, 2000; Huang 2001; Heil 2004; Luo *et al.* 2008; Wang *et al.* 2021*a*) or by a fixed upstream pressure (Jensen & Heil 2003; Stewart *et al.* 2010; Liu *et al.* 2012). To facilitate mechanistic understanding of this asymmetric two-dimensional (2-D) system, attention has also focused on (semi-rational) one-dimensional (1-D) reductions that exploit a long-wavelength approximation and a flow profile assumption to derive closed systems of equations. One such 1-D model was derived by Stewart, Waters & Jensen (2009) for flow driven by a fixed upstream pressure, and has subsequently been applied to a flux-driven system (Xu *et al.* 2013, 2014; Stewart 2017). Across these various approaches the asymmetric finite-length collapsible channel has been demonstrated to exhibit a wide variety of interesting phenomena, including several distinct families of self-excited oscillations driven by fundamentally different mechanisms (Luo *et al.* 2008; Stewart *et al.* 2009; Stewart 2017), multiple steady flow configurations (Luo & Pedley 2000; Heil 2004; Stewart 2017; Wang *et al.* 2021*a*), flow-limitation and pressure-drop limitation (Luo & Pedley 2000), divergent instabilities and slamming events (Stewart 2010; Stewart *et al.* 2010; Xu, Billingham & Jensen 2013; Xu & Jensen 2015).

In this study we model the flexible portion of the wall as a nonlinearly elastic beam with a large pre-tension, extending our previous work involving a beam with no pre-tension (Luo *et al.* 2008; Wang *et al.* 2021*a*,*b*). This approach facilitates comparison with earlier computational studies with simpler wall models (Luo & Pedley 1996, 2000) and lower-order reductions of the flow (Stewart 2017). In particular, we consider a range of approaches including a full 2-D computational model, a linear stability eigensolver and a 1-D model (§ 2). Similar to previous studies, this system always exhibits at least one steady state and can exhibit a multiplicity of steady states for some parameter regimes (§ 3). It emerges that when the external pressure is fixed to relatively low values, this system exhibits a steady state that is mostly inflated along the collapsible segment (termed the upper branch), while for larger values of the external pressure, the system instead exhibits a highly collapsed steady configuration (termed the lower branch). Similar to our previous work (Wang *et al.* 2021*a*,*b*), we show that both the upper and lower branch steady states can become unstable to distinct modes of self-excited oscillation, and use our models to map out the unstable regions of the parameter space (§ 4). Finally, we elucidate the mechanisms of both low- and high-frequency normal modes growing from the lower branch of static solutions (§ 5) and oscillations growing from the upper branch of static solutions (§ 6). A second family of oscillations growing from the upper branch of static solutions is summarised in the Appendix.

2. The model

We consider a 2-D rigid channel of uniform width D conveying an incompressible Newtonian fluid with uniform density ρ and viscosity μ.

Similar to our previous work (Wang *et al.* 2021*a*,*b*), we consider a flow driven by a fixed inlet flux Q (per unit length in the out-of-plane direction) with a fixed (reference) pressure P imposed along the channel outlet.
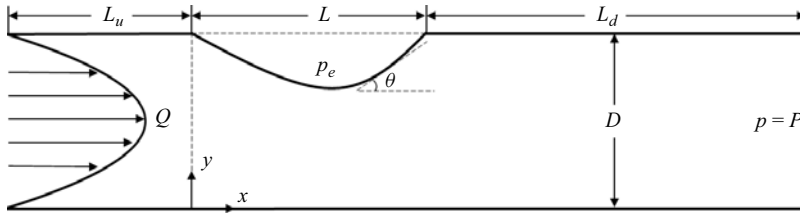
Figure 1. Sketch of the model set-up in dimensional variables.

A segment of length L of the upper wall of the channel is replaced by a plane-strain elastic beam of initial thickness $\mathcal{H}$; prior to deformation this beam is assumed to be flat and parallel to the entire rigid wall. The resulting lengths of the upstream and downstream rigid segments are denoted as L_u and L_d, respectively, so the total length of the collapsible channel is denoted as $L_0 = L_u + L + L_d$.

A Cartesian coordinate system is established in the channel where x measures the distance along the entire rigid wall (from the junction between the upstream rigid segment and the compliant segment) and y measures the normal distance from this wall oriented into the channel; see set-up sketched in figure 1.

The elastic upper wall is modelled as a massless beam with extensional stiffness e_λ and bending stiffness e_b. This beam is held under a constant pre-tension T and subject to a uniform external pressure p_e. In this study we focus on a parameter regime where the influence of the pre-tension dominates the other restoring effects.

The flat, undeformed elastic beam is parameterised by a coordinate l ($0 \leqslant l \leqslant L$). An arbitrary point on the beam at $l = l_a$ is mapped to $\boldsymbol{x}_b = (x_b(l_a, t), y_b(l_a, t))$ in the Cartesian coordinate system after deformation, where t denotes time.

The 2-D fluid velocity field is denoted as $\boldsymbol{u} = (u(x, y, t), v(x, y, t))$ and the fluid pressure is denoted at $p(x, y, t)$.

The material (Lagrangian) velocity of the elastic beam is denoted as

$$\boldsymbol{u}_b(l, t) = \frac{\partial \boldsymbol{x}_b(l, t)}{\partial t}; \tag{2.1}$$

we project this material velocity to the current (Eulerian) description to derive the spatial velocity of the beam $\boldsymbol{u}_s(x, y, t)$, defined such that

$$\boldsymbol{u}_b(l, t) = \boldsymbol{u}_s(x_b(l, t), y_b(l, t), t). \tag{2.2}$$

We scale all lengths on the channel width D, velocities on Q/D and time on D^2/Q. We also scale the pressure on an inertial scale relative to the outlet value, where we write

$$\tilde{p} = \frac{p - P}{\rho Q^2 / D^2}; \tag{2.3}$$

dimensionless variables are indicated with the same symbol but with a tilde. The corresponding dimensionless parameters governing the dynamics of the fluid and the beam take the form

$$\tilde{Re} = \frac{\rho Q}{\mu}, \quad \tilde{p}_e = \frac{p_e D^2}{\rho Q^2}, \quad \tilde{T} = \frac{TD}{\rho Q^2}, \quad \tilde{c}_\lambda = \frac{e_b D}{\rho Q^2}, \quad \tilde{c}_\kappa = \frac{e_\lambda}{\rho Q^2 D}, \tag{2.4}$$

denoting the Reynolds number of the flow, the dimensionless external pressure, the dimensionless pre-tension, extensional and bending stiffness of the elastic beam, respectively. Furthermore, the geometry of the channel is described by the dimensionless

1024 A58-4

lengths of each segment:

$$\tilde{L}_u = \frac{L_u}{D}, \quad \tilde{L} = \frac{L}{D}, \quad \tilde{L}_d = \frac{L_d}{D}. \tag{2.5}$$

We henceforth drop the tildes for all the variables and parameters.

2.1. *Governing equations for the full 2-D model*

The dimensionless governing equations for the fluid are the incompressible Navier–Stokes equations in the form

$$\nabla \cdot \boldsymbol{u} = 0, \tag{2.6a}$$

$$\frac{\partial \boldsymbol{u}}{\partial t} + (\boldsymbol{u} \cdot \nabla)\boldsymbol{u} = \nabla \cdot \boldsymbol{\sigma}. \tag{2.6b}$$

The corresponding Newtonian stress tensor $\boldsymbol{\sigma}$ in (2.6b) takes the form

$$\boldsymbol{\sigma} = -p\boldsymbol{I} + Re^{-1}\left(\nabla \boldsymbol{u} + \nabla \boldsymbol{u}^{\mathrm{T}}\right), \tag{2.6c}$$

where $\boldsymbol{I}$ is the identity tensor and the superscript $^{\mathrm{T}}$ denotes the transpose operator.

2.2. *Boundary conditions*

At a given time t the flexible wall profile is the line of material points

$$\{(x_b(l, t),\, y_b(l, t)) : 0 \leqslant l \leqslant L\}. \tag{2.6d}$$

Our numerical method (see §2.4) can handle highly deformed beam configurations, including cases where the wall profile is a multi-valued function of x (see the discussion in Luo & Pedley 1996). However, for all the examples considered below, it emerges that the x component of the beam profile, x_b, is a one-to-one function of l for a given t, so the dependency on l can be eliminated and the corresponding profile of the wall can (in this case) be written in the form $y = h(x, t) = y_b(x_b^{-1}(x, t), t)$.

For the viscous fluid, we assume no-slip conditions along the rigid walls and continuity of velocity between the fluid and elastic beam in the form

$$\boldsymbol{u} = \boldsymbol{0}, \qquad (y = 0;\ y = 1,\ -L_u \leqslant x \leq 0,\ L \leqslant x \leqslant L + L_d), \tag{2.6e}$$

$$\boldsymbol{u} = \boldsymbol{u}_s, \qquad (y = h(x, t),\ 0 \leqslant x \leqslant L). \tag{2.6f}$$

For notational convenience, we denote $h(x, t) = 1$ along $-L_u \leqslant x \leqslant 0$ and $L \leqslant x \leqslant L + L_d$.

The governing equations for the massless elastic beam are obtained by considering conservation of linear and angular momentum (Cai & Luo 2003; Wang *et al.* 2021a). In turn, these can be expressed in the form of a balance of tangential and normal stress across the beam in the form

$$c_\kappa \frac{\kappa}{\lambda} \frac{\partial(\lambda\kappa)}{\partial l} + c_\lambda \frac{1}{\lambda}\frac{\partial\lambda}{\partial l} + (\boldsymbol{\sigma}\boldsymbol{n}) \cdot \boldsymbol{t} = 0, \tag{2.6g}$$

$$-c_\kappa \frac{1}{\lambda}\frac{\partial}{\partial l}\left(\frac{1}{\lambda}\frac{\partial(\lambda\kappa)}{\partial l}\right) + c_\lambda\kappa(\lambda - 1) + \kappa T + (\boldsymbol{\sigma}\boldsymbol{n}) \cdot \boldsymbol{n} = p_e, \tag{2.6h}$$

where we have the constraints

$$\frac{\partial x_b}{\partial l} = \lambda\cos\theta, \qquad \frac{\partial y_b}{\partial l} = \lambda\sin\theta, \qquad \frac{\partial\theta}{\partial l} = \lambda\kappa; \tag{2.6i}$$

here λ is the principal stretch of the elastic beam, κ is the in-plane curvature and θ is the angle between the rigid wall and the tangent vector of the deformed elastic wall
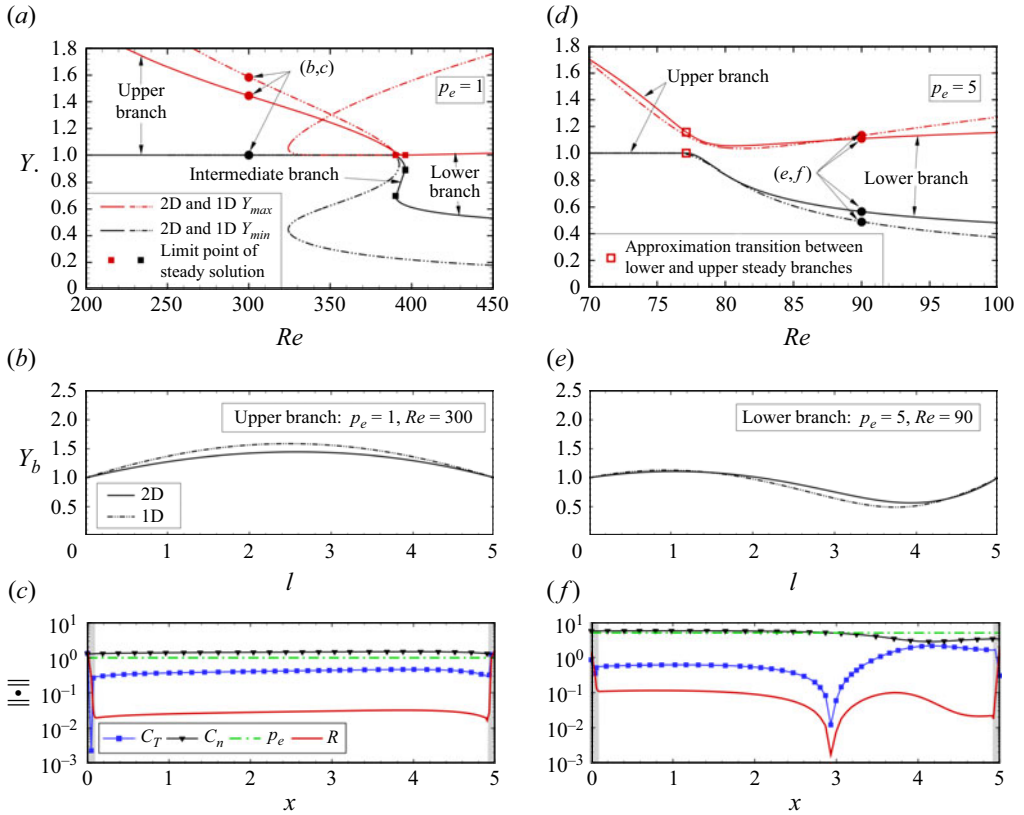
Figure 2. Steady solutions of the fluid-beam system computed using the full 2-D simulations, plotting (*a*) the maximal and minimal steady wall deflection as a function of Reynolds number for $p_e = 1$; (*b*) the spatial profile of the steady wall as a function of the material coordinate l for $p_e = 1$, $Re = 300$; (*c*) terms in the reduced normal stress balance (2.7*a*) as a function of the streamwise coordinate x for $p_e = 1$, $Re = 300$; (*d*) the maximal and minimal steady wall deflection as a function of Reynolds number for $p_e = 5$; (*e*) the spatial profile of the steady wall as a function of the material coordinate l for $p_e = 5$, $Re = 90$; (*f*) terms in the reduced normal stress balance (2.7*a*) as a function of the streamwise coordinate x for $p_e = 5$, $Re = 90$. The upper and lower branch limit points for $p_e = 1$ are denoted as filled squares in (*a*), while the approximate transition between the upper and lower branch for $p_e = 5$ is indicated as an open square in (*d*). The point denoted with a circle in (*a*) corresponds to the profiles in (*b,c*), while the point denoted with a circle in (*d*) corresponds to the profiles in (*e,f*).

(see figure 1). The normal and tangential unit vectors of the deformed elastic beam are denoted as $\boldsymbol{n}$ and $\boldsymbol{t}$, respectively.

In this paper we focus on a parameter regime where the elastic response of the beam is dominated by the longitudinal pre-tension, where the normal stress balance (2.6*h*) can be approximated as

$$R \equiv C_T + C_n - p_e \approx 0, \tag{2.7a}$$

where we define the contributions due to the pre-tension and the normal fluid stress as

$$C_T \equiv \kappa T, \qquad C_n \equiv (\boldsymbol{\sigma}\boldsymbol{n}) \cdot \boldsymbol{n}. \tag{2.7b}$$

We quantify the residual R and the size of these individual terms in figure 2.

We note that in this study we have neglected the contribution of the wall inertia in the stress balances in the beam and so this prevents flutter-like instabilities found in previous

1024 A58-6

studies (e.g. Luo & Pedley 1998) that onset due to two-way fluid–structure interaction. In addition, the two ends of the elastic beam are fixed and clamped to the rigid segments upstream and downstream, where we have

$$x_b(0, t) = 0, \qquad y_b(0, t) = 1, \qquad \theta(0, t) = 0, \qquad (2.8a)$$
$$x_b(L, t) = L, \qquad y_b(L, t) = 1, \qquad \theta(L, t) = 0. \qquad (2.8b)$$

In this fluid-driven system the inlet flow has a prescribed parabolic profile $u(-L_u, y, t) = 6y(1 - y)$, $v(-L_u, y, t) = 0$, with maximal velocity $3/2$ along the centreline. The corresponding fluid pressure along the channel inlet is denoted as $p_{in}(y, t) = p(-L_u, y, t)$; in simulations we track temporal variations in the cross-sectionally averaged upstream pressure $\overline{p}_{in}(t)$ (see details below).

In the computations we impose that the flow across the channel outlet ($x = L + L_d$) is stress free, which for a sufficiently long downstream segment, is indistinguishable from a zero pressure condition (see discussion in Jensen & Heil 2003).

In the simulations reported below we track the dynamics of the unsteady system using several spatial and temporal measures. Firstly, we introduce the cross-sectionally averaged fluid pressure (denoted with an overbar), defined as

$$\overline{p}(x, t) = \frac{1}{h(x, t)} \int_0^{h(x,t)} p(x, y, t) \, \mathrm{d}y \qquad (-L_u \leqslant x \leqslant L + L_d). \qquad (2.9a)$$

In particular, across the channel inlet $\overline{p}_{in}(t) = \overline{p}(-L_u, t)$. Secondly, we consider the time trace of the wall pressure at the mid-point of the compliant segment in the reference configuration ($l = (1/2)L$), which we denote as

$$p_{mid}(t) = p\left(x_b\left(\tfrac{1}{2}L, t\right), y_b\left(\tfrac{1}{2}L, t\right), t\right). \qquad (2.9b)$$

Thirdly, we consider the maximal and minimal elastic wall deflections denoted as

$$y_{max}(t) = \max_l(y_b(l, t)) \geqslant 1, \qquad y_{min}(t) = \min_l(y_b(l, t)) \leqslant 1. \qquad (2.9c)$$

Additionally, the spatially averaged wall deflection over the compliant segment is denoted as

$$\overline{y}_b = \frac{1}{L} \int_0^L y_b(l, t) \, \mathrm{d}l. \qquad (2.9d)$$

Finally, we use the cross-sectionally averaged pressure distribution (2.9a) to construct the spatially averaged pressure gradient along each compartment of the channel, such that

$$\overline{\nabla p_u}(t) = \frac{1}{L_u} \int_{-L_u}^0 \frac{\partial \overline{p}(x, t)}{\partial x} \, \mathrm{d}x = \frac{1}{L_u} (\overline{p}(0, t) - \overline{p}(-L_u, t)), \qquad (2.9e)$$

$$\overline{\nabla p_c}(t) = \frac{1}{L} \int_0^L \frac{\partial \overline{p}(x, t)}{\partial x} \, \mathrm{d}x = \frac{1}{L} (\overline{p}(L, t) - \overline{p}(0, t)), \qquad (2.9f)$$

$$\overline{\nabla p_d}(t) = \frac{1}{L_d} \int_L^{L+L_d} \frac{\partial \overline{p}(x, t)}{\partial x} \, \mathrm{d}x = \frac{1}{L_d} (\overline{p}(L_d, t) - \overline{p}(L, t)). \qquad (2.9g)$$

For each of these temporal measures, we can then further compute the corresponding time-averaged value over one period of oscillation, which we denote with a superscript

(avg); a function $f(t)$ averaged over a period τ takes the form

$$f^{(avg)} = \frac{1}{\tau} \int_{t_0}^{t_0+\tau} f(t) \, \mathrm{d}t, \qquad (2.10a)$$

where t_0 is some reference time.

In our previous work (Wang *et al.* 2021*a*) we also quantified the dynamics of self-excited oscillations using analysis of the corresponding energy budget of the system. We do not reproduce this derivation here but note that the rate of working of the upstream pressure can be expressed as

$$\mathcal{P}(t) = - \left[\int_0^1 pu \, \mathrm{d}y \right]_{x=-L_u}^{x=L+L_d}. \qquad (2.10b)$$

In the particular case where the cross-channel profile of the upstream driving pressure $p(-L_u, y, t)$ is independent of y (which is a good approximation for the examples illustrated below), the rate of working of the upstream pressure $\mathcal{P}(t) \approx \overline{p}_{in}(t)$ since the inlet flow rate is fixed and the outlet pressure is zero. Hence, the work done by the upstream pressure over a period of oscillation is given by

$$\mathcal{P}^{(avg)} \approx \overline{p}_{in}^{(avg)}. \qquad (2.10c)$$

2.3. *Steady solutions*

We denote the steady flow velocity, pressure and Newtonian stress tensor as $U(x, y)$, $P(x, y)$ and $\boldsymbol{\Sigma}(x, y) = -P(x, y)\boldsymbol{I} + Re^{-1}(\nabla U(x, y) + \nabla U(x, y)^{\mathrm{T}})$ respectively. The corresponding stretch and curvature of the steady beam are denoted as $\Lambda(l)$ and $K(l)$, respectively, while the steady beam deflection is denoted as $\boldsymbol{X}_b(l) = (X_b(l), Y_b(l))$ and the angle between the steady beam and rigid wall is denoted as $\Theta(l)$. Therefore, the equations governing the steady system are

$$\nabla \cdot U = 0, \qquad (2.11a)$$

$$(U \cdot \nabla) U = \nabla \cdot \left(- P\boldsymbol{I} + Re^{-1} \left(\nabla U + \nabla U^{\mathrm{T}} \right) \right), \qquad (2.11b)$$

subject to boundary conditions

$$U = 0 \quad (y = 0; \; y = 1, \; -L_u \leqslant x \leqslant 0, \; L \leqslant x \leqslant L + L_d; \; y = H(x), \; 0 \leqslant x \leqslant L), \qquad (2.11c)$$

and the governing equations for the steady beam are

$$c_\kappa \frac{K}{\Lambda} \frac{\partial (\Lambda K)}{\partial l} + c_\lambda \frac{1}{\Lambda} \frac{\partial \Lambda}{\partial l} + (\boldsymbol{\Sigma} N) \cdot T = 0, \qquad (2.11d)$$

$$-c_\kappa \frac{1}{\Lambda} \frac{\partial}{\partial l} \left(\frac{1}{\Lambda} \frac{\partial (\Lambda K)}{\partial l} \right) + c_\lambda K(\Lambda - 1) + KT + (\boldsymbol{\Sigma} N) \cdot N = p_e, \qquad (2.11e)$$

where T and N are the corresponding tangential and normal unit vectors to the steady beam. In addition, the geometric constraints on the steady beam take the form

$$\frac{\partial X_b}{\partial l} = \lambda \cos \Theta, \qquad \frac{\partial Y_b}{\partial l} = \Lambda \sin \Theta, \qquad \frac{\partial \Theta}{\partial l} = \Lambda K. \qquad (2.11f)$$

Similar to the unsteady system, we construct the steady wall profile in the form $y = H(x)$, and define $H(x) = 1$ along $-L_u \leqslant x \leqslant 0$ and $L \leqslant x \leqslant L + L_d$ for notational convenience. We form the steady cross-stream averaged pressure distribution

$$\overline{P}(x) = \frac{1}{H(x)} \int_0^{H(x)} P(x, y) \, dy \qquad (-L_u \leqslant x \leqslant L + L_d), \qquad (2.12a)$$

alongside the steady inlet pressure $\overline{P}_{in} = \overline{P}(-L_u)$. Similarly, the spatially averaged steady pressure gradient along each compartment can be written as

$$\overline{\nabla P}_u = \frac{1}{L_u}(\overline{P}(0) - \overline{P}(-L_u)), \qquad (2.12b)$$

$$\overline{\nabla P}_c = \frac{1}{L}(\overline{P}(L) - \overline{P}(0)), \qquad (2.12c)$$

$$\overline{\nabla P}_d = \frac{1}{L_d}(\overline{P}(L_d) - \overline{P}(L)). \qquad (2.12d)$$

We also construct the maximal and minimal channel widths, defined as

$$Y_{max} = \max_l(Y_b(l)) \geqslant 1, \qquad Y_{min} = \min_l(Y_b(l)) \leqslant 1, \qquad (2.12e)$$

respectively.

Finally, at a given time t we compute the difference between the current wall profile and the steady profile, written as

$$\Delta y_b(l, t) = y_b(l, t) - Y_b(l), \qquad (2.12f)$$

the difference between the steady and unsteady cross-stream averaged pressure distributions in the form

$$\overline{\Delta p}(x, t) = \overline{p}(x, t) - \overline{P}(x), \qquad (2.12g)$$

as well as the excess (cross-sectionally averaged) streamwise pressure gradients along each compartment

$$\overline{\delta p_u}(t) = \overline{\nabla p}_u(t) - \overline{\nabla P}_u, \qquad (2.12h)$$

$$\overline{\delta p_c}(t) = \overline{\nabla p}_c(t) - \overline{\nabla P}_c, \qquad (2.12i)$$

$$\overline{\delta p_d}(t) = \overline{\nabla p}_d(t) - \overline{\nabla P}_d. \qquad (2.12j)$$

2.4. *Numerical methods*

Following Wang *et al.* (2021a) (see also Luo *et al.* 2008) we use a finite element method with a six-node triangular mesh to solve the fluid-beam system (2.6). In particular, the flow is described using an Arbitrary Lagrangian–Eulerian method for the domain under the elastic wall with an adaptive mesh with rotational spines, whereas the domain under the rigid wall is described using an Eulerian method with a fixed mesh (Luo *et al.* 2008). We employ a Galerkin approach to construct weighting functions for the fluid momentum equations (2.6a, 2.6b) and the normal stress balance in the beam (2.6h), but instead use a Petrov–Galerkin weighted residual method for the tangential stress balance across the beam (2.6g) and the constraints (2.6i). For unsteady problems, an implicit finite-difference scheme is used for time stepping, where a frontal approach and a Newton–Raphson iteration scheme are used at each time step to assemble and solve the discretised matrix equations.

To initialise the unsteady numerical solutions, we apply a small perturbation by using the corresponding steady state with a 1 % increment in c_λ.

A mesh of 36 657 six-node triangular elements and 140 three-node elements is used for the numerical simulations. Convergence tests were reported in Wang *et al.* (2021a).

2.5. *Eigenvalue problem*

To further our understanding of the system, we also construct a linear stability eigensolver around a given steady state of the system. This eigensolver is constructed using the method described by Hao *et al.* (2016), where we add a small perturbation to the basic state in the form

$$f(x, y, t) = F(x, y) + \varepsilon \hat{f}(x, y, t), \quad g(l, t) = G(l) + \varepsilon \hat{g}(l, t), \tag{2.13}$$

where $\varepsilon \ll 1$, $f(x, y, t)$ and $g(l, t)$ represent the fluid and beam related variables, while $F(x, y)$, $G(l)$ and $\hat{f}(x, y, t)$, $\hat{g}(l, t)$ are the corresponding steady state and first-order perturbation variables, respectively. To derive the corresponding eigenvalue problem for this perturbed system, we neglect all terms of $O(\epsilon^2)$ and assume that these first-order perturbations take the wave-like form

$$\hat{f}(x, y, t) = \tilde{f}(x, y)\mathrm{e}^{-i\omega t} + \left(\tilde{f}(x, y)\mathrm{e}^{-i\omega t}\right)^*, \quad \hat{g}(l, t) = \tilde{g}(l)\mathrm{e}^{-i\omega t} + \left(\tilde{g}(l)\mathrm{e}^{-i\omega t}\right)^*, \tag{2.14}$$

where $\tilde{f}(x, y)$ and $\tilde{g}(l)$ are the complex amplitude functions and $\omega = \omega_r + i\omega_i$ is the complex frequency; here ω_r is the oscillation frequency of the perturbation and ω_i is the corresponding growth rate. The system is unstable when $\omega_i > 0$, asymptotically stable when $\omega_i < 0$ and is neutrally stable for $\omega_i = 0$. The superscript $*$ denotes a complex conjugate.

Substituting (2.13) and (2.14) into the governing equations (2.6), we obtain the eigenvalue problem for the coupled system in the form

$$\nabla \cdot \tilde{\boldsymbol{u}} = 0, \tag{2.15a}$$

$$-i\omega\tilde{\boldsymbol{u}} + (\boldsymbol{U} \cdot \nabla)\tilde{\boldsymbol{u}} + (\tilde{\boldsymbol{u}} \cdot \nabla)\boldsymbol{U} = \nabla \cdot \left[-\tilde{p}\boldsymbol{I} + Re^{-1}\left(\nabla\tilde{\boldsymbol{u}} + \nabla\tilde{\boldsymbol{u}}^{\mathrm{T}}\right)\right], \tag{2.15b}$$

subject to boundary conditions (projected to the steady state)

$$\tilde{\boldsymbol{u}} = \boldsymbol{0} \qquad\qquad (y = 0; \, y = 1, \, -L_u \leqslant x \leqslant 0, \, L \leqslant x \leqslant L + L_d), \tag{2.15c}$$

$$\tilde{\boldsymbol{u}} + \left(\tilde{x}_b\frac{\partial \boldsymbol{U}}{\partial x} + \tilde{y}_b\frac{\partial \boldsymbol{U}}{\partial y}\right) = \tilde{\boldsymbol{u}}_s(x) \qquad (y = H, \, 0 \leqslant x \leqslant L), \tag{2.15d}$$

where $\tilde{\boldsymbol{u}}_s(x) = -i\omega\tilde{\boldsymbol{x}}_b(X_b^{-1}(x))$ is the linearised spatial wall velocity. The linearised governing equations for the elastic beam take the form

$$c_\kappa\left[\frac{\tilde{\kappa}}{\Lambda}\frac{\mathrm{d}(\Lambda K)}{\mathrm{d}l} + \frac{K}{\Lambda}\frac{\mathrm{d}(\tilde{\lambda}K + \Lambda\tilde{\kappa})}{\mathrm{d}l} - \frac{\tilde{\lambda}K}{\Lambda^2}\frac{\mathrm{d}(\Lambda K)}{\mathrm{d}l}\right] + c_\lambda\left(\frac{1}{\Lambda}\frac{\mathrm{d}\tilde{\lambda}}{\mathrm{d}l} - \frac{\tilde{\lambda}}{\Lambda^2}\frac{\mathrm{d}\Lambda}{\mathrm{d}l}\right)$$
$$+ \left[\left(\tilde{\boldsymbol{\sigma}} + \tilde{x}_b\frac{\mathrm{d}\boldsymbol{\Sigma}}{\mathrm{d}x} + \tilde{y}_b\frac{\mathrm{d}\boldsymbol{\Sigma}}{\mathrm{d}y}\right)\boldsymbol{N}\right] \cdot \boldsymbol{T} = 0, \tag{2.15e}$$

$$- c_\kappa\left[\frac{1}{\Lambda}\frac{\mathrm{d}}{\mathrm{d}l}\left(\frac{1}{\Lambda}\frac{\mathrm{d}(\Lambda\tilde{\kappa} + \tilde{\lambda}K)}{\mathrm{d}l} - \frac{\tilde{\lambda}}{\Lambda^2}\frac{\mathrm{d}(\Lambda K)}{\mathrm{d}l}\right) - \frac{\tilde{\lambda}}{\Lambda^2}\frac{\mathrm{d}}{\mathrm{d}l}(\frac{1}{\Lambda}\frac{\mathrm{d}(\Lambda K)}{\mathrm{d}l})\right]$$
$$+ c_\lambda\left[K\tilde{\lambda} + \tilde{\kappa}(\Lambda - 1)\right] + \tilde{\kappa}T + \left[\left(\tilde{\boldsymbol{\sigma}} + \tilde{x}_b\frac{\mathrm{d}\boldsymbol{\Sigma}}{\mathrm{d}x} + \tilde{y}_b\frac{\mathrm{d}\boldsymbol{\Sigma}}{\mathrm{d}y}\right)\boldsymbol{N}\right] \cdot \boldsymbol{N} = 0, \tag{2.15f}$$

subject to the constraints

$$\frac{d\tilde{x}_b}{dl} = -\Lambda\tilde{\theta}\sin(\Theta) + \tilde{\lambda}\cos(\Theta), \quad \frac{d\tilde{y}_b}{dl} = \Lambda\tilde{\theta}\cos(\Theta) + \tilde{\lambda}\sin(\Theta), \quad \frac{d\tilde{\theta}}{dl} = \Lambda\tilde{\kappa} + \tilde{\lambda}K.$$

(2.15g)

We note that these perturbation eigenfunctions are all projected back to the corresponding steady state, which leads to a number of additional terms in the linearised governing equations involving spatial gradients of the steady flow vector U and the steady stress tensor Σ; see Wang (2019) for details. We note that although these extra terms are crucial to the mechanism of instability in many classical hydrodynamic stability problems (e.g. Kelvin–Helmholtz and Rayleigh–Taylor instabilities; see Drazin 2002), in this case their influence is relatively small.

Following Hao *et al.* (2016), we solve the eigenvalue problem (2.15) numerically using an Arnoldi-Frontal method. We characterise the output of the eigensolver through the growth rate ω_i and frequency ω_r of the normal modes, alongside the corresponding spatial profiles of the eigenfunction (which has both real and imaginary parts).

2.6. *Reduced 1-D model*

We also consider a reduced 1-D model of the same collapsible channel system, first derived by Stewart *et al.* (2009) and subsequently used by a number of authors (e.g. Stewart *et al.* 2010; Xu *et al.* 2013, 2014; Xu & Jensen 2015; Stewart 2017). The derivation of this model assumes long-wavelength deformations, a von Karman–Pohlhausen approximation for the flow profile (i.e. everywhere parabolic), encodes the reduced form of the normal stress balance (2.6h) and neglects axial stretching of the wall (so motion of the wall is always normal to the rigid wall). In this model the system is described in terms of the width of the collapsible segment $h(x, t)$ and the axial flux along the channel $q(x, t)$, where the governing equations can be written in the form

$$h_t + q_x = 0, \quad q_t + \frac{6}{5}\left(\frac{q^2}{h}\right)_x = Th h_{xxx} - \frac{12}{Re}\frac{q}{h^2},$$

(2.16a)

across $0 \leqslant x \leqslant L$, subject to

$$q(0, t) = 1, \quad Th_{xx}(L, t) = -L_d\left[q_t + \frac{12}{Re}q\right], \quad h(0, t) = h(L, t) = 1. \quad (2.16b)$$

This system is solved numerically using finite-difference methods constructed by Stewart *et al.* (2009), using Newton iteration to construct the steady states and a semi-implicit time-stepping scheme to compute unsteady profiles. Furthermore, we use an analogue of our linear stability eigensolver (constructed by Stewart 2017) to test the stability of steady states, constructing the growth rate and frequency of perturbations, as well as their corresponding complex eigenfunctions.

2.7. *Parameter choices*

Throughout this study we fix the lengths of the three segments of the channel (L_u, L and L_d) and the initial thickness of the elastic beam $\mathcal{H}$ by setting

$$L_u = L = 5, \quad L_d = 30, \quad \mathcal{H} = 0.01.$$

(2.17)

This choice of downstream segment is sufficiently long so that outflow is unidirectional.

We focus attention on a parameter regime where the pre-tension in the wall strongly dominates the other elastic effects, meaning that the system is analogous to earlier membrane models (e.g. Luo & Pedley 1996, 2000). In this case we choose $c_\lambda = 10$, $c_\kappa = (\mathcal{H}^2/12)c_\lambda$ and $T = 3$; we confirm in figure 2 that the dominant elastic effect is indeed the restoring effect of the pre-tension for these parameters.

To examine the steady and unsteady behaviour of the system, we choose the external pressure in the range $0 < p_e \leqslant 10$ and focus on laminar (non-turbulent) flows in the range $0 < Re < 800$.

In what follows we summarise the predictions of our models, including a brief overview of both the steady (see § 3) and unsteady behaviour (see § 4) and a more detailed study of particular families of oscillation (see §§ 5, 6, Appendix).

3. Steady solutions

In order to elucidate the steady behaviour of the system, figure 2 presents computations of (2.11), summarising the behaviour for both $p_e = 1$ (figure 2a–c) and $p_e = 5$ (figure 2d–f), through the maximal and minimal steady wall deflection as a function of the Reynolds number (i.e. Y_{max} and Y_{min}, figure 2a,d), alongside typical spatial profiles of the steady wall (figure 2b,e) and the components of the normal stress balance (figure 2c,f). For the two selected values of the external pressure, the elastic wall is inflated for low Reynolds numbers as the fluid pressure is significantly larger than the external pressure (figure 2b). However, this bulging gradually reduces as the Reynolds number increases and the system becomes collapsed, where the elastic beam is drawn towards the entire rigid wall as the fluid pressure locally reduces through the Bernoulli effect (figure 2e). For large p_e, this collapse is monotonic (figure 2d), while for lower p_e, there is a narrow range of Reynolds numbers where the system exhibits three steady states for the same parameter values (e.g. for $p_e = 1$, this corresponds to the range $390.13 \lesssim Re \lesssim 396.1$, figure 2a), before transitioning into an entirely collapsed state for larger Re. The region of the parameter space with three coexisting steady states is shown as the narrow red region in the parameter space in figure 3(a). In what follows, we term the inflated steady state (evident for low Re) as the upper branch of steady solutions (figure 2b), and term the collapsed steady state (evident for large Re) as the lower branch of steady solutions (figure 2e). Although the transition between these upper and lower branch static states is clear when there is an intermediate branch between them, this distinction is more subjective when the two branches merge smoothly into one another. In the latter case we approximate the transition as the threshold value of Re where the minimal width of the channel wall just drops below the end value i.e. $Y_{min} < 1$. The point where this occurs for $p_e = 5$ is labelled as an open square on figure 2(d) ($Re \approx 77.14$), and we trace this transition point through the parameter space as the red dotted line figure 3. Such regions with multiple steady solutions have previously been identified in this collapsible channel system (Luo & Pedley 2000; Wang *et al.* 2021*a*; Herrada *et al.* 2022) and the associated limit points have been shown to play a key role in organising the dynamical system (Xu *et al.* 2013; Stewart 2017; Wang *et al.* 2021*a*). However, it emerges below that the region of the parameter space with multiple steady solutions is very narrow and well away from the neutral stability curves of interest (see the narrow red region in figure 3a).

The corresponding steady behaviour of the 1-D model (2.16) is also shown in figure 2, plotting traces of the maximal and minimal steady beam deflection (dot-dashed lines in figure 2a,d) and typical spatial wall profiles (dot-dashed lines in figure 2b,e). For relatively large external pressures where the transition between upper and lower steady states occurs
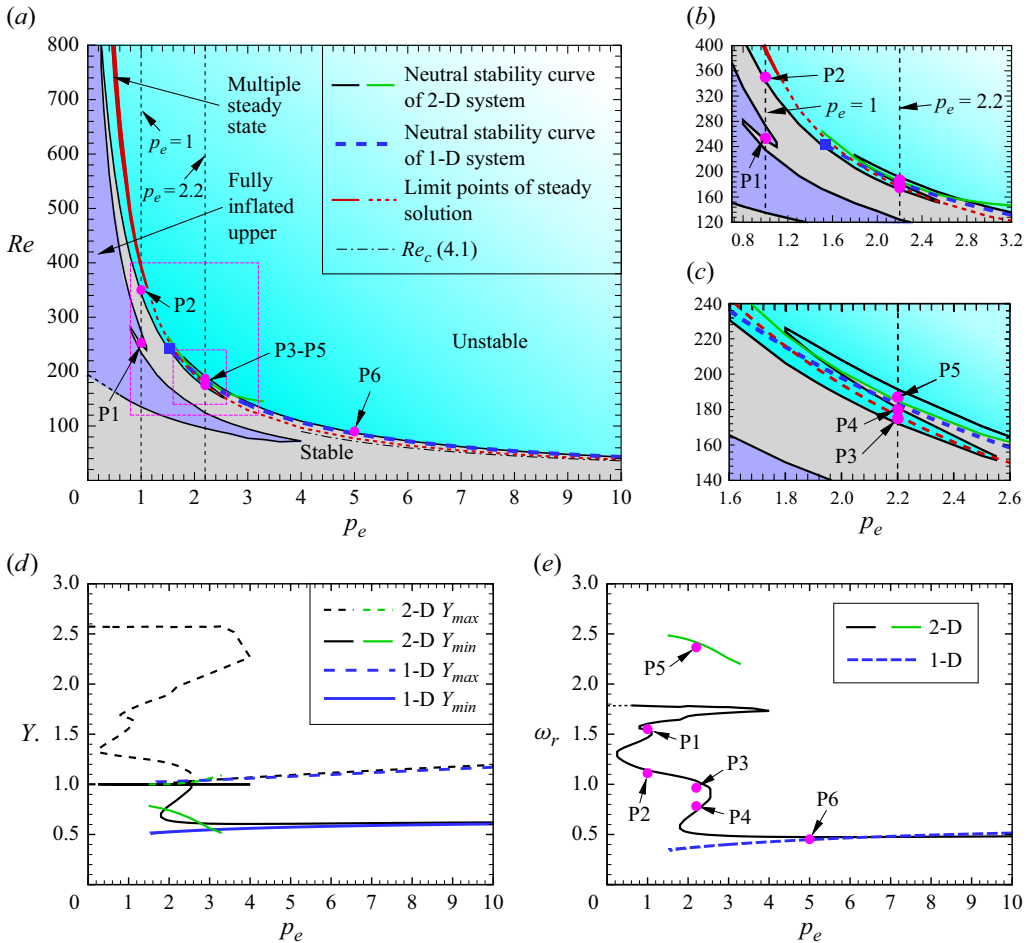
Figure 3. Overview of the stability of the system for $T = 3$ as a function of the external pressure p_e, plotting (*a*) the neutral stable curves of the system in terms of the critical Reynolds number Re; (*b,c*) a close-up of the neutral stability curves in the two regions marked by dashed magenta dashed boxes in (*a*); (*d*) maximal (Y_{max}) and minimal (Y_{min}) width of the corresponding steady channel along the neutral stability curves; (*e*) the oscillation frequency along the neutral stability curves. In panels (*a–c,e*) the neutral stability curves are shown as the solid black line (low-frequency oscillations) and the solid green line (high-frequency oscillation). The narrow red region in (*a*) corresponds to the region of parameter space with three coexisting steady solutions. The red dashed line in (*a–c*) indicates the approximate transition between upper and lower branch steady states. The operating points P1–P6 are shown as filled magenta circles. The corresponding predictions from the 1-D model are shown in blue, while the asymptotic approximation to the 1-D model in the limit of large external pressure is shown as a black dot-dashed line.

for modest Reynolds numbers (where we expect the flow profile assumption of the 1-D model to be appropriate), we observe excellent agreement between the two approaches (e.g. $p_e = 5$, figure 2*d*). However, we note that the differences become increasingly marked as the Reynolds number increases (figure 2*d*) and are most evident when the external pressure is low and the transition between upper and lower steady states occurs for much larger Reynolds numbers (figure 2*a*); even in this case the predictions of the 1-D model are qualitatively similar to the full computations, predicting the upper branch of steady solutions and its limit point reasonably well, but the intermediate and lower steady branches are much more collapsed than the full computations (figure 2*a*).

In order to determine the balance of terms in the normal stress balance on the elastic beam (2.6*h*), figures 2(*c*) and 2(*f*) illustrates spatial profiles of the terms identified in the reduced normal stress balance (2.7*a*) for these two choices of external pressure, showing that in both cases the dominant balance is between the external pressure (p_e) and the normal stress exerted by the fluid across the interior of the wall profile (C_n), while the role of the restoring effect of membrane tension (C_T) is smaller but still significantly larger than the other components of the normal stress contained in the residual (R); the additional contributions to the elastic response of the beam are essentially negligible in this parameter regime; note that the cusps in figures 2(*c*) and 2(*f*) arise because we are taking the absolute value of a quantity that crosses zero at some spatial location. We also note very narrow boundary layers adjacent to the rigid segments (shaded in grey) where the balance is very different and the role of bending resistance becomes dominant as the beam adjusts to satisfy the prescribed slope condition (2.8); these boundary layers are relatively passive and do influence the wall profile away from the edges.

We now examine the stability of these steady solutions to self-excited oscillations, first providing an overview of the stability across the parameter space (§ 4), before examining oscillations growing from both the lower branch of steady states (§ 5) and the upper branch of steady states (§ 6), which we term 'lower branch oscillations' and 'upper branch oscillations', respectively. Additionally, a second family of instabilities growing from the upper branch of steady solutions is discussed in the Appendix, which we term 'fully upper branch' instabilities.

4. Unsteady solutions

In order to examine the stability of the upper and lower branches of steady solutions (described in § 3), we add a small perturbation to the steady profile and examine the resulting unsteady response. As is typical in hydrodynamic stability theory, the system is deemed stable if the unsteady solution converges back to the corresponding steady state and unstable if the perturbation grows into another state. The critical state between stable and unstable traces a curve through the parameter space; we trace these neutral stability curves using the global stability eigensolver (§ 4.1). We further consider fully nonlinear simulations within the unstable zones to elucidate the corresponding limit cycles of these oscillatory instabilities (§ 4.2).

4.1. *Neutral stability curves*

Figure 3 presents an overview of the stability of the collapsible channel system, plotting the neutral stability curves in the parameter space spanned by external pressure p_e and Reynolds number *Re*, holding the wall pre-tension fixed at $T = 3$; the full space is shown in figure 3(*a*), while panels (*b,c*) provide enlargements of particular regions (magenta dashed boxes in figure 3*a*). Tracing in terms of the external pressure, the corresponding maximal (Y_{max}) and minimal (Y_{min}) channel widths of the steady profile at neutral stability are plotted in figure 3(*d*), while the neutrally stable oscillation frequencies are plotted in figure 3(*e*).

For large external pressures, the system exhibits a neutral stability curve where the critical Reynolds number decreases with increasing p_e (see figure 3*a*), where the corresponding steady channel is highly collapsed (consistent with the lower branch of steady solutions, figure 3*d*) and the frequency of the neutrally stable oscillation is $O(1)$ (figure 3*e*). The corresponding nonlinear growth of these lower branch oscillations is discussed in § 5. The onset of this lower branch oscillatory instability is also well predicted by the corresponding 1-D model (2.16), where the neutral stability curve, static

profiles and oscillation frequencies all agree well with the full computations (figure 3d,e). Furthermore, we also see strong agreement with the asymptotic solution of this 1-D model in the limit of large p_e (Stewart 2017), where the critical Reynolds number for the onset of oscillatory instability takes the approximate form

$$Re_c \approx \frac{12}{p_e} L_d; \tag{4.1}$$

this curve is shown as the black dot-dashed line in figure 3(a), which overlaps closely with the other approaches. Hence, the 1-D model is a strong predictor of the oscillatory behaviour along this lower branch of steady solutions.

As the external pressure decreases, the computed neutral stability curve becomes increasingly complicated. The lower branch oscillatory structure is eventually suppressed at a limit point ($p_e \approx 1.80$), beyond which the system transitions to upper branch steady states. In this case the limit point is one of a pair (the other being at $p_e \approx 2.55$) that form a sigmoid in the neutral stability curve across a short range of external pressures ($1.80 \lesssim p_e \lesssim 2.55$), where the system exhibits three possible critical Reynolds numbers (see close-up of the parameter space in figure 3c). Across these three neutrally stable solutions, the corresponding steady profile becomes increasingly inflated as the Reynolds number decreases (figure 3d), while the corresponding oscillation frequency gradually increases (figure 3e). We explore the nonlinear development of several oscillatory modes in this regime in §4.2. We note that these limit points are not associated with those of the underlying steady system (those limit points only arise for much larger Reynolds numbers, shown as the shaded narrow red region in figure 3a), but our approximate demarcation line between upper and lower branches (red dashed line) does pass almost perfectly through the second limit point at $p_e \approx 2.55$, suggesting that this point is indeed associated with a change from a lower to an upper branch steady configuration. Note also that the 1-D model (2.16) does not predict this three branch behaviour, and instead the corresponding neutral stability curve persists in the lower branch configuration until eventually terminating when the system reaches a limit point associated with the end of the lower steady branch (this point is indicated with a filled blue square in figures 3a and 3b).

Returning to the neutral stability curve from the full computations, we observe that as the external pressure decreases below the lower limit point ($p_e \approx 2.55$), the critical Reynolds number again approximately increases with the inverse of p_e, although the corresponding steady profile is almost entirely inflated and so the dynamics of the self-excited oscillations growing from this upper branch are quite different to the lower branch. We consider the nonlinear development of oscillatory normal modes growing from this upper branch in §6.

However, across the range of external pressures with three neutrally stable solutions we detect a second, entirely separate, neutral stability curve associated with an instability of much higher frequency growing from the lower branch of steady solutions (marked as the green line in figure 3). Across a narrow range of external pressures ($1.5 \lesssim p_e \lesssim 3.3$) this high-frequency normal mode is the primary global instability, i.e. more unstable than the low-frequency mode. A narrow range of the external pressures where the collapsible channel system is dominated by high-frequency normal modes was also evident in the predictions from the 1-D model (Stewart 2017). This high-frequency family of modes is described in more detail in §5.2.

For this low value of the membrane tension, it emerges that the upper branch instability is more complicated than previously reported by Wang *et al.* (2021a), where the instability was eventually suppressed as the external pressure decreased below a threshold (Wang *et al.* 2021b). In the present case the system exhibits a second form of upper branch
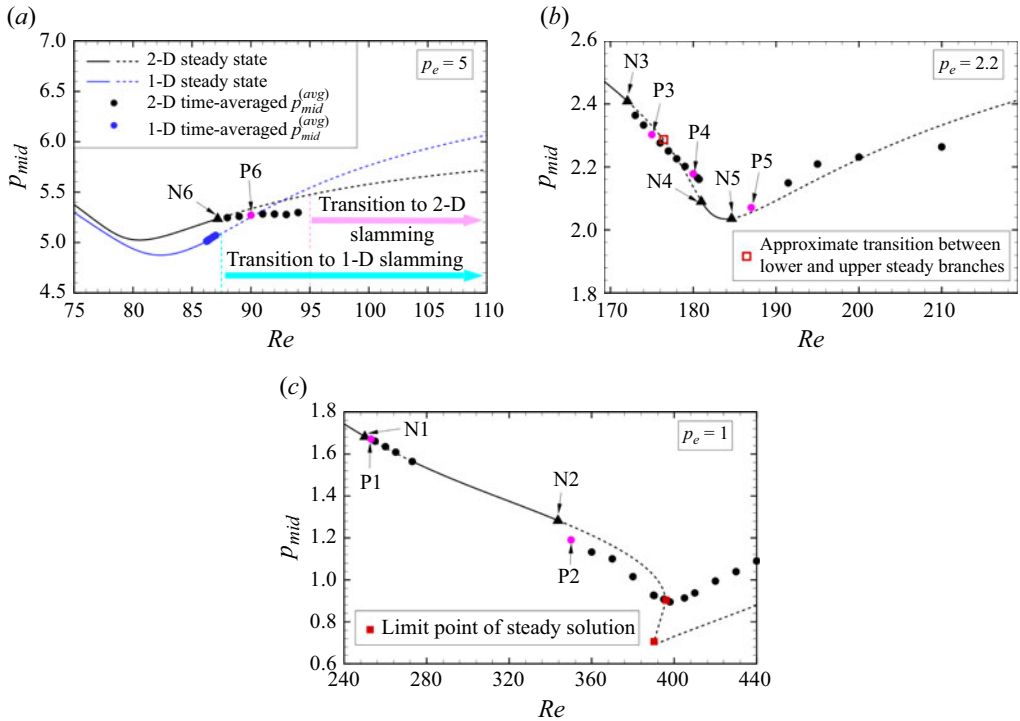
Figure 4. Overview of the parameter space calculated using full computations of the 2-D model, plotting both the steady and time-averaged mid-point pressures as a function of the Reynolds number for (*a*) $p_e = 5$, (*b*) $p_e = 2.2$ and (*c*) $p_e = 1$. In each panel the time-averaged mid-point pressures for oscillations growing from the upper and lower steady branches are denoted as filled black and magenta circles, respectively, while the stable and unstable steady states are denoted with solid and dashed lines, respectively. The approximate demarcation between the upper and lower steady states is marked with an open red square in panel (*b*). The corresponding steady and time-averaged mid-point pressures calculated from the 1-D model (2.16) are denoted in blue with the same line styles.

instability for even lower values of the external pressure, where the dynamics of the resulting self-excited oscillations are substantially different. The corresponding neutral stability curve for this instability is evident in the parameter space in figure 3, manifesting as a large tongue (coloured in purple) sitting below the neutral stability curve discussed above, connecting smoothly to it at $p_e \approx 0.25$, $Re \approx 805.82$. Furthermore, this new two-branch neutral stability curve is confined to low external pressures by a limit point at $p_e \approx 4.02$, beyond which this new form of upper branch instability is absent. We consider an oscillatory normal mode in this unstable range in the Appendix.

4.2. *Traces through the parameter space*

The parameter space shown in figure 3 demonstrates that the system is unstable to at least three distinct forms of self-excited oscillation (termed lower branch, upper branch and fully upper branch oscillations).

In order to show how these different families of instabilities fit together with their corresponding static profiles, figure 4 presents several slices through the parameter space for a fixed external pressure. In particular, we construct bifurcation diagrams as a function of Reynolds number by plotting the time-averaged mid-point pressure on the compliant wall, $p_{mid}^{(avg)}$, for three external pressures, namely $p_e = 5$ (figure 4*a*), $p_e = 2.2$ (figure 4*b*)
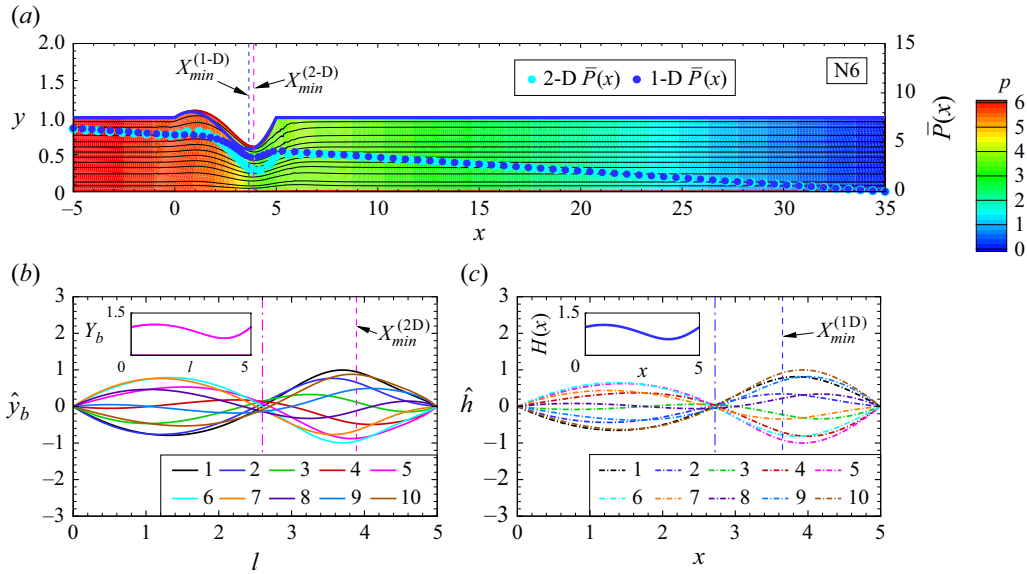
Figure 5. Neutrally stable low-frequency self-excited oscillations originating from the lower branch of steady solutions for $p_e = 5$, considering the prediction of the 2-D model at point N6 ($Re = 87.17$) alongside the prediction from the 1-D model ($Re = 86.25$): (*a*) steady flow-field and pressure contours from the 2-D model, (*b*) eigenfunction wall profile plotted at 10 snapshots over a period of oscillation from the 2-D model, (*c*) eigenfunction wall profile plotted for 10 snapshots over a period of oscillation from the 1-D model. The eigenfunctions in (*b*,*c*) are normalised on the maximum of the modulus of the (complex-valued) wall profile. The blue and cyan filled circles in (*a*) are the corresponding cross-stream averaged steady pressure distributions for the one- and 2-D models, respectively. The dashed lines in (*a*–*c*) indicate the spatial location of the minimal channel width, while the dot-dashed lines in (*a*–*c*) indicate the point where the wave profile is approximately pinned; in each case the magenta lines are from the 2-D model, while the blue lines are from the 1-D model. The insets in (*b*,*c*) show the steady wall profile from 2-D and 1-D models, respectively.

and $p_e = 1$ (figure 4*c*) alongside the corresponding values computed from the steady simulations (where stable and unstable configurations are plotted as solid and dashed lines, respectively).

For relatively large external pressures ($p_e = 5$, figure 4*a*), no upper branch or fully upper branch instability is present and the system becomes unstable to low-frequency lower branch oscillations beyond a critical Reynolds number ($Re \approx 87.17$, labelled N6). The corresponding transition point for the 1-D model is slightly lower ($Re \approx 86.25$), but the neutrally stable eigenfunctions show excellent qualitative agreement (see figure 5). These oscillations grow in amplitude as the Reynolds number increases (figure 4*a*) and eventually the system exhibits highly nonlinear 'slamming' oscillations for $Re \gtrsim 95$ for the full simulations (marked by pink arrow in figure 4*a*). Fully nonlinear simulations of the 1-D model (2.16) exhibit qualitatively similar dynamics, although the growth in amplitude of the saturated limit cycle is much more pronounced as the Reynolds number increases, and so the 'slamming' oscillations onset much closer to the neutral stability curve ($Re \gtrsim 87.5$ in this case).

For an external pressure chosen within the interval that exhibits three pieces of the same neutral stability curve ($p_e = 2.2$, figure 4*b*), the system now exhibits two families of oscillatory behaviour. For low Reynolds numbers, the system exhibits an unstable interval between $Re \approx 172.05$ (labelled N3) and $Re \approx 180.97$ (labelled N4). The corresponding steady profile of the channel is completely inflated for lower Reynolds numbers across this range, but becomes partially collapsed as the Reynolds number increases.

These oscillations are similar in character to the upper branch oscillations described in our previous work (Wang *et al.* 2021*a*), and while their eventual termination as the Reynolds number increases is not directly associated with the limit point of the steady solutions, it is driven by the collapse of the underlying steady state (similar to examples shown in Wang *et al.* 2021*b*). Indeed this normal mode growing from the upper branch of steady solutions stabilises close to our approximate demarcation between upper and lower steady states (open red square in figure 4*b*). The mechanism of these upper branch instabilities is explored in § 6. As the Reynolds number increases, the system subsequently destabilises again for $Re \approx 184.63$ (labelled N5); this transition is analogous to the onset of lower branch oscillations described for $p_e = 5$, but corresponds to a different normal mode of the system with a much larger oscillation frequency (figure 3*e*); the temporal dynamics of these high-frequency lower branch oscillations are explored in § 5.2.

For a relatively low external pressure ($p_e = 1$, figure 4*c*), the system again exhibits two intervals of oscillatory behaviour. In this case the oscillatory instability first onsets for $Re \approx 250.01$ (labelled N1), where the corresponding steady state is very highly inflated (figure 3*d*). As the Reynolds number increases, this oscillatory mode subsequently stabilises at $Re \approx 273.02$, where the base state is still very highly inflated. Hence, the dynamics of these fully upper oscillations is different to the upper branch oscillations described previously and are explored in more detail in the Appendix. As the Reynolds number increases further, the system eventually destabilises again for $Re \approx 343.67$ (labelled N2), in a manner almost identical to the upper branch oscillations. For this external pressure, the system exhibits a range of Reynolds numbers with three coexisting steady states. For these parameters, the corresponding lower branch of steady solutions is always unstable to oscillations, and the associated limit cycle merges with that of the upper branch oscillations across the interval with multiple steady states; a similar merging of the upper and lower branch limit cycles was observed by Wang *et al.* (2021*b*).

We now proceed to explore the nonlinear dynamics of the lower branch oscillations (§ 5), the upper branch oscillations (§ 6) and the fully upper branch oscillations (Appendix) by considering 12 particular cases (labelled on figure 4), elucidating the underlying mechanism of instability by examining both the neutrally stable eigenfunctions (operating points N1–N6) and the unsteady dynamics nearby (operating points P1–P6). Movies of the unsteady oscillations at points P1–P6 are provided as supplementary material available at https://doi.org/10.1017/jfm.2025.10860.

5. Lower branch instabilities

Lower branch instabilities divide into two types: low-frequency oscillations (§ 5.1) and high-frequency oscillations (§ 5.2). We describe each type by analysing both neutrally stable eigenfunctions and nonlinear dynamical profiles, constructing a description of the mechanism of instability in each case.

5.1. *Low-frequency normal modes*

These lower branch oscillations are analogous to the low-frequency lower branch oscillations described by Stewart (2017) using the (empirical) 1-D model (2.16). In order to validate these predictions against full 2-D computations, figure 5 explores the dynamics of neutrally stable low-frequency lower branch oscillations at operating point N6. Firstly, we plot streamlines and pressure contours of the steady flow profile and the cross-sectionally averaged pressure distribution (figure 5*a*) alongside the corresponding steady wall profile from the 1-D model (shown in blue, plotted at the critical Reynolds number $Re \approx 86.25$ for the same external pressure). These steady wall profiles compare well between the

two approaches, both exhibiting an outward bulge at the upstream end of the compliant compartment, and substantial collapse toward the downstream end in a so-called mode-2 configuration (two extrema in the wall profile), while the locations of the minimal channel thickness are also very similar (figure 5*a*). The corresponding steady pressure profiles also show good agreement, both exhibiting a local minimum toward the downstream end of the compliant segment. Snapshots of the eigenfunction wall profile at 10 equally spaced points over a period of neutrally stable oscillation are shown for both the full simulations (figure 5*b*) and the 1-D model (figure 5*c*). Over a period of oscillation these neutrally stable eigenfunction profiles agree very well between the two approaches, exhibiting an almost identical amplitude (when normalised according to the same protocol), where each eigenfunction wall profile has two extrema (mode-2) with a larger amplitude toward the downstream end of the collapsible segment. Interestingly, in both approaches all the oscillatory wall profiles exhibit zero amplitude at a consistent spatial location just downstream of the centre of the compliant compartment (i.e. both real and imaginary parts of the eigenfunction wall profile are close to zero simultaneously, indicated by the dot-dashed lines in figures 5*b* and 5*c*); this zero-crossing point is distinct from the global minimum of the steady profile (which is considerably closer to the downstream end of the compliant channel, see dashed line in figures 5*a* and 5*c*), and so the steady state is not dictating the structure of the eigenfunction (in contrast to the high-frequency instabilities discussed in § 5.2). Although we note small variations in the location of this zero-crossing for 2-D simulations (figure 5*b*), for the 1-D model, this point is almost perfectly constant (figure 5*c*), suggesting that the perturbation wall profile is approximately a standing wave. In summary, this figure suggests that the neutrally stable perturbation wall profile is approximately a standing wave, pinned both at the ends of the compliant segment and also at an interior point near the centre.

In order to explore the dynamics of the fully developed limit cycles originating from this oscillatory normal mode, figure 6 illustrates temporal and spatial profiles of the flow over a period of self-excited oscillation for a Reynolds number just above neutral (operating point P6). A time trace of the mid-point wall pressure p_{mid} is shown in figure 6(*a*), illustrating three periods of oscillation, while figure 6(*b–k*) shows streamlines and pressure contours at the 10 points marked on this trace. For each snapshot, we also plot the corresponding spatial profile of the difference between the (cross-stream averaged) instantaneous pressure and the steady pressure (i.e. $\overline{\Delta p}(x, t)$, figure 6*b–k*). The flow profiles are almost perfectly laminar throughout the oscillation and exhibit little cross-stream pressure variation (the colours are almost independent of *y*), in agreement with the assumptions of the 1-D model (figure 6*b–k*). In all cases the unsteady pressure gradient in the upstream rigid segment is essentially identical to the corresponding steady flow (the excess pressure profile is spatially uniform), while in the downstream rigid segment the unsteady pressure distribution varies almost linearly compared with the steady pressure distribution (the excess pressure profile is linear; see cyan triangles in figure 6*b–k*). However, across the compliant segment variations in the pressure are more significant, in some cases almost half of the magnitude of the corresponding steady driving pressure ($\overline{P_{in}}$). We consider these quantities further in figure 7.

Over an oscillation the wall retains the mode-2 wall profile with almost no longitudinal motion of the material points, while the location of maximal constriction also remains approximately fixed ($x \approx 3.9$). As expected, at instances where the channel is highly collapsed the fluid pressure upstream of the point of maximal constriction becomes raised to become almost equal to the driving pressure (see colour contours in figure 6*e–h*). Furthermore, as the channel collapses the pressure close to the point of maximal constriction falls considerably compared with the steady value (figure 6*d–g*), but still
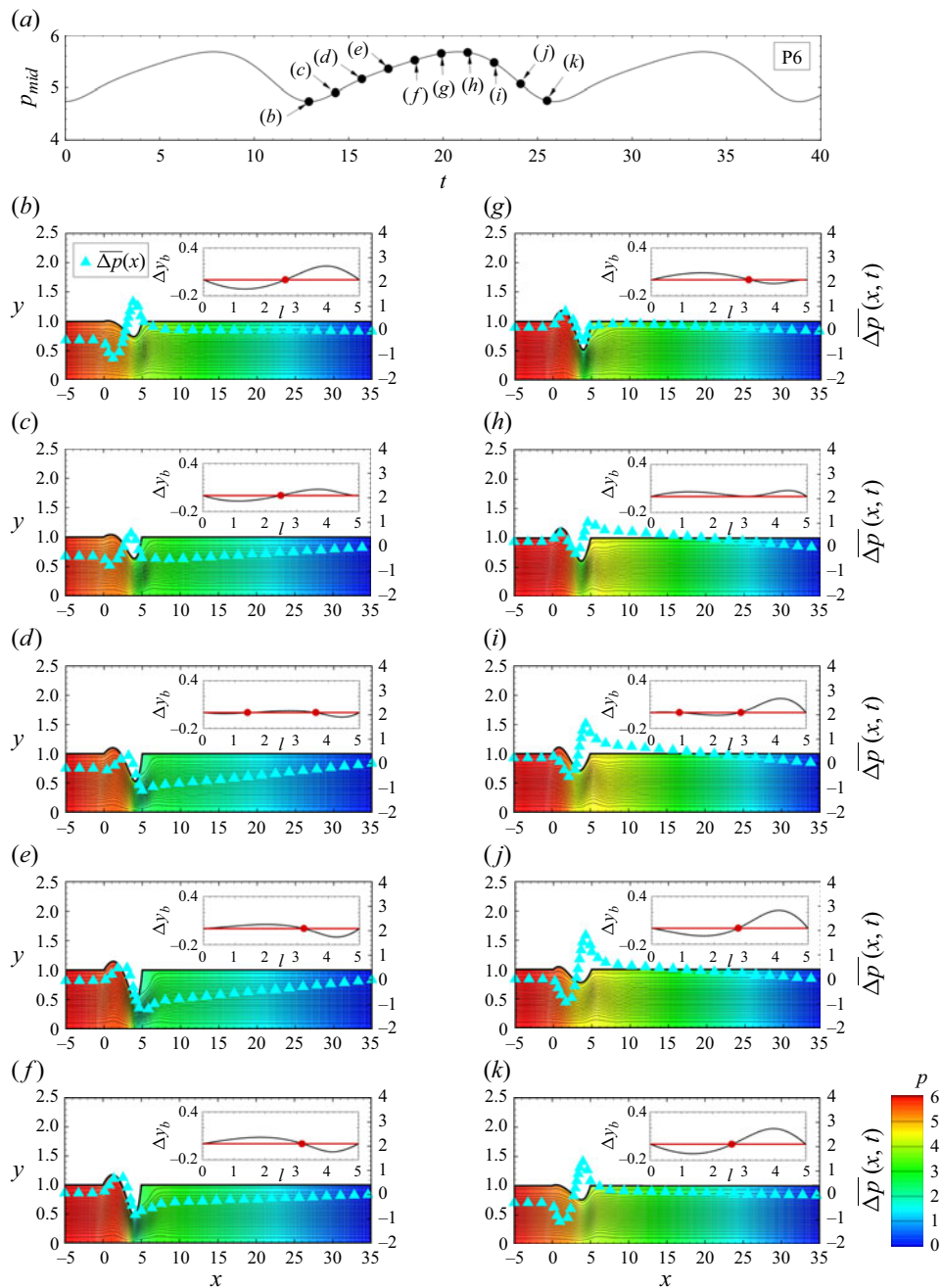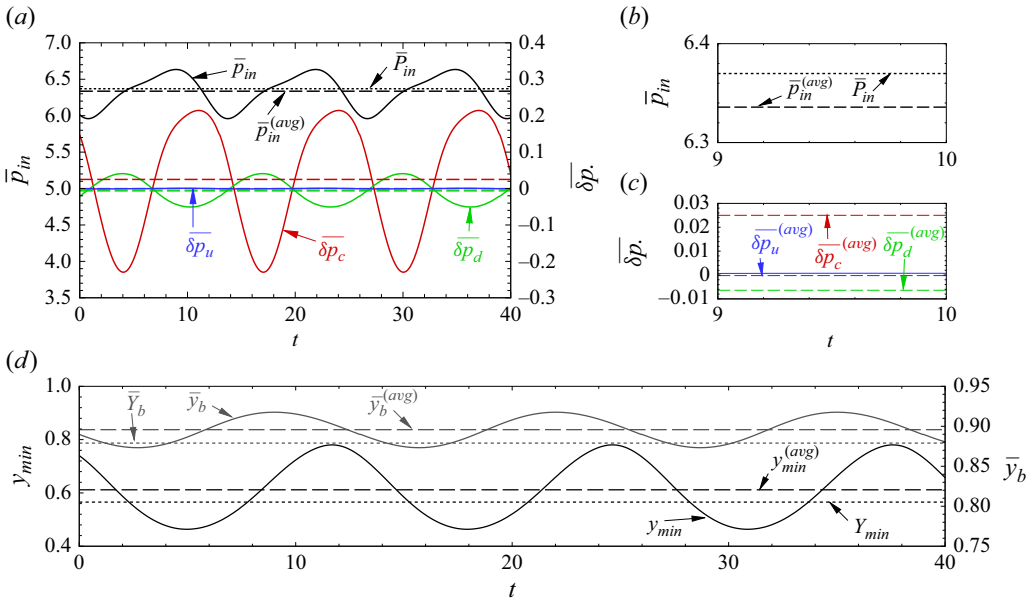
Figure 6. Fully developed low-frequency self-excited oscillations growing from the lower branch of steady solutions predicted by the 2-D model at operating point P6 ($p_e = 5$, $Re = 90$): (*a*) time trace of the wall mid-point pressure $p_{mid}(t)$ over three periods of oscillation, (*b–k*) streamlines and pressure contours of the instantaneous flow field at 10 equally spaced time instances over one period (corresponding times marked in panel (*a*)). The cyan filled triangles in (*b–k*) illustrate the excess (cross-stream averaged) pressure compared with the steady pressure ($\overline{\Delta p}$). The insets in (*b–k*) show the difference between the instantaneous wall profile compared with the steady flow (Δy_b).

Figure 7. Fully developed low-frequency self-excited oscillations growing from the lower branch of steady solutions at operating point P6 ($p_e = 5$, $Re = 90$), including (*a*) the time trace of the cross-sectionally averaged inlet pressure ($\overline{p}_{in}$, black curve) and the excess pressure gradient compared with the steady ($\delta p.$) in the upstream (blue curve), compliant (red curve) and downstream (green curve) segments; (*b*) a close-up of the time trace of the cross-sectionally averaged inlet pressure; (*c*) a close-up of the time trace of the excess pressure gradients in each segment; (*d*) the time trace of the minimal channel width (left axis) and the spatially averaged channel width (right axis). Note the corresponding time-averaged and steady values are denoted as dashed and dotted lines in panels (*a–d*).

remains well in excess of the outlet pressure and so there is no flow reversal in the downstream rigid segment. We also note that, for this relatively low Reynolds number, there is also no substantial vorticity wave downstream of the compliant segment, a prominent feature of earlier models in flux-driven oscillations in collapsible channel flows (e.g. Luo & Pedley 1996; Luo *et al.* 2008; Huang *et al.* 2021). Hence, the resulting oscillation predicted by the full 2-D computations exhibits many of the features encoded into the 1-D model (2.16), and so it is no surprise that this 1-D model predicts quantitatively similar oscillations. The dynamics of the oscillation can be seen more clearly in the movie for operating point P6 provided as supplementary material.

Stewart (2017) used an approximate 1-D model to describe the mechanism of these low-frequency lower branch oscillations, showing that on average over a period the compliant wall is less collapsed than the corresponding steady wall profile, which releases the energy needed to sustain the oscillation. In order to validate these predictions using the full 2-D system, figure 7 compares time traces of several pertinent quantities to their corresponding steady values, including the (cross-sectionally averaged) upstream driving pressure (figure 7*a,b*), the (spatially averaged) streamwise pressure gradient along each segment of the channel (figure 7*a,c*) and both the minimal width of the channel and the average wall position (figure 7*d*). Over a period of oscillation the mean upstream pressure is reduced compared with the corresponding steady value, meaning that (on average) the oscillatory flow is working less hard than the steady flow, making it energetically favourable (figure 7*a,b*). Furthermore, over a period of oscillation there is no significant change in the pressure gradient along the upstream and downstream rigid segments of the channel

compared with the steady flow (figure 7*a*,*c*). However, the corresponding time-averaged pressure gradient along the compliant segment is significantly increased (less negative, figure 7*a*,*c*), corroborating our observation that overall the flow is working less hard in the oscillatory state. This reduction is also evident in the spatially averaged beam deflection, where, in agreement with Stewart (2017), on average the beam profile is less collapsed over a period compared with the steady state and so stored elastic energy is released to sustain the oscillation (figure 7*d*). Hence, this figure demonstrates that our fully nonlinear 2-D simulations agree well with the earlier predictions of the 1-D model, showing that on average the fully developed oscillation reduces the mean constriction of the channel and increases the pressure gradient along the compliant segment. In the online supplementary material we also demonstrate that the cross-channel profiles of the velocity components and the pressure are consistent with the assumptions of the 1-D model. In summary, figure 7 shows that the mechanism of these low-frequency self-excited oscillations growing from the lower branch of steady solutions is similar to that predicted by the 1-D model of Stewart (2017), where the fully developed oscillation causes the collapsed wall to open slightly (on average), releasing stored elastic energy to sustain the instability.

5.2. *High-frequency normal modes*

In addition to these low-frequency normal modes, Stewart (2017) also reported a family of high-frequency normal modes that grow from the lower branch of steady solutions. These normal modes are typically more stable than the low-frequency oscillations, but Stewart (2017) elucidated a small region of the parameter space where one of these high-frequency modes is the primary global instability of the system. These oscillations were described using an asymptotic approximation in the limit of large external pressure, where it was shown that the steady channel becomes highly constricted, pinning the perturbation wall profile at the location of the global minimum of the steady profile, and the corresponding perturbation flow can thus be effectively divided into two pieces, each of which is characterised by the number of extrema in the perturbation wall profile. In order to compare these predictions to those of the full 2-D model, in figure 8 we consider the dynamics at operating point N5, a neutral stability point within the small range of parameter space where the high-frequency response is the primary global instability (see figure 3). As expected, the steady state is collapsed (figure 8*a*), although the maximal constriction is relatively modest ($Y_{min} \approx 0.67$ at $X_{min} \approx 3.54$). However, even in this case the corresponding perturbation wall profiles (figure 8*b*) are standing waves pinned at the point of maximal constriction, with two (one) extrema (extremum) upstream (downstream) of the point of maximal constriction, in good qualitative agreement with one of the high-frequency oscillatory modes found using the 1-D model (Stewart 2017). Hence, in this case the perturbation wall profile exhibits two zero crossings with almost coincident real and imaginary parts (red dashed line in figure 8*b*). In order to further elucidate the oscillatory dynamics, figure 8(*c*) traces the spatial location of the local minimum of the perturbation wall profile, demonstrating how it gradually transverses upstream following a path that takes two periods of oscillation. In summary, this figure demonstrates that the family of high-frequency oscillatory modes predicted by the 2-D simulations exhibit strong qualitative agreement with the earlier predictions of the 1-D model, where the wall profile is approximately a standing wave pinned at the point of maximal constriction of the steady profile.

For brevity we do not include snapshots of the streamlines and pressure contours, but the unsteady dynamics at operating point P5 are shown in the online supplementary material and in the accompanying movie. Interestingly, the excess cross-stream averaged pressure
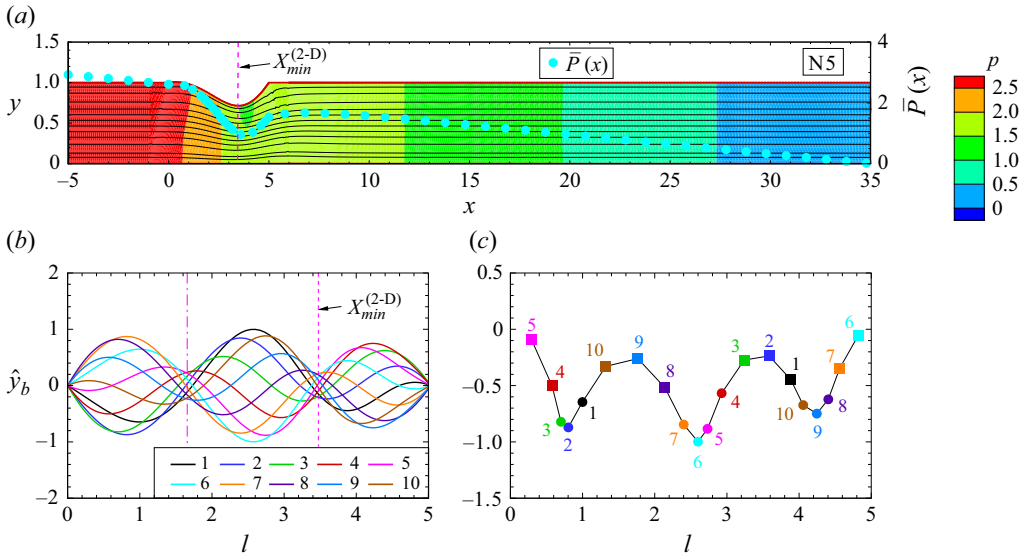
Figure 8. Neutrally stable high-frequency self-excited oscillations originating from the lower branch of steady solutions for $p_e = 2.2$ from the 2-D model at point N5 ($Re = 184.63$): (*a*) steady flow-field and pressure contours, (*b*) eigenfunction wall profile plotted at 10 snapshots over a period of oscillation from the 2-D model, (*c*) spatial location and value of the local minimum of the perturbation wall profile over a period of oscillation. The eigenfunctions in (*b,c*) are normalised on the maximum of the modulus of the (complex-valued) wall profile. The cyan filled circles in (*a*) are the corresponding cross-stream averaged steady pressure distributions. The red dashed lines in (*a,b*) indicate the spatial location of the minimal channel width, while the magenta dot-dashed line in (*b*) indicates the point where the wave profile is approximately pinned.

$(\overline{\Delta p}(x, t))$ now typically exhibits three extrema over the compliant segment rather than two for the low-frequency oscillations (see figure 5).

In order to elucidate the mechanism of these high-frequency instabilities, in figure 9 we trace the (cross-sectionally averaged) upstream driving pressure (figure 9*a,b*), the corresponding difference in the (spatially averaged) pressure gradient between unsteady and steady flows in each compartment (figure 9*a,c*) as well as both the spatially averaged and minimal beam deflections (figure 9*d*). In this case the effect is much more modest and harder to extract: the time-averaged upstream driving pressure is increased compared with the steady value (figure 9*b*), while the other trends are similar to the lower branch oscillations in that the spatially averaged pressure is again increased compared with the steady profile (red dashed line in figure 9*a,c*) and the time-averaged beam deflection is decreased compared with the steady value (figure 9*d*). Hence, this figure demonstrates that the mechanism of the high-frequency lower branch instability is much more difficult to discern, exhibiting some overlap with the low-frequency lower branch oscillations but the observations are not fully consistent. However, given the relatively small differences between the steady and time-averaged unsteady profiles, more investigation is required to fully quantify the mechanism. In online supplementary material we again show that the cross-channel profiles of the velocity components and pressure are consistent with the assumptions of the 1-D model.

6. Upper branch instabilities

Oscillatory instabilities originating from the (inflated) upper branch of steady solutions were previously described by Wang *et al.* (2021*a*) and Herrada *et al.* (2022), using different
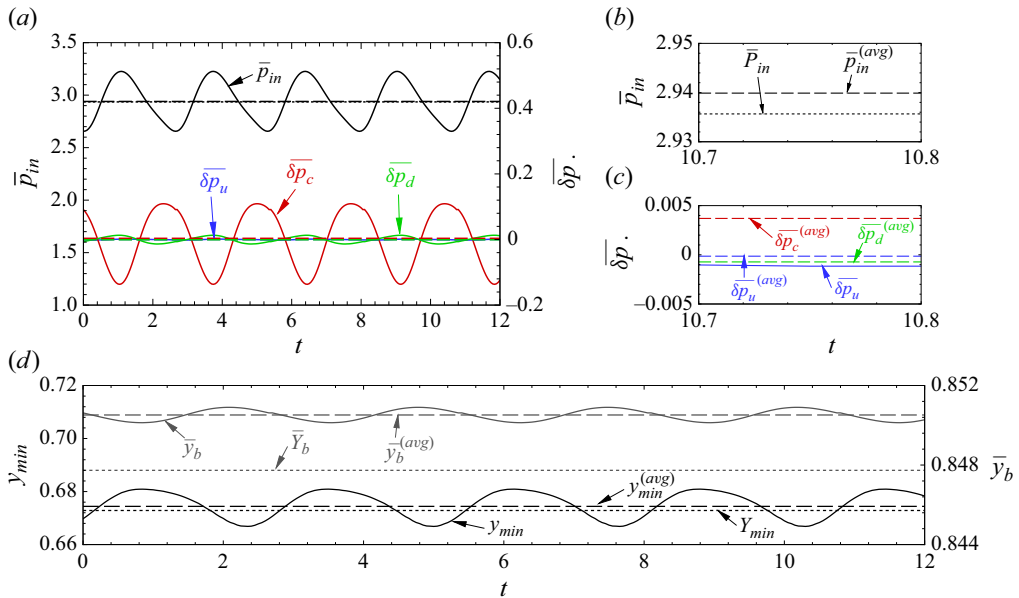
Figure 9. Fully developed high-frequency self-excited oscillations growing from the lower branch of steady solutions at operating point P5 ($p_e = 2.2$, $Re = 187$), including (*a*) the time trace of the cross-sectionally averaged inlet pressure ($\overline{p}_{in}$, black curve) and the excess pressure gradient compared with the steady (δp.) in the upstream (blue curve), compliant (red curve) and downstream (green curve) segments; (*b*) a close-up of the time trace of the cross-sectionally averaged inlet pressure; (*c*) a close-up of the time trace of the excess pressure gradients in each segment; (*d*) the time trace of the minimal channel width (left axis) and the spatially averaged channel width (right axis). Note the corresponding time-averaged and steady values are denoted as dashed and dotted lines in panels (*a*–*d*).

wall models. Although both studies noted periodic upstream propagation of a surface wave along the flexible wall, the underlying mechanism is still unclear. Interestingly, such upper branch instabilities are entirely absent from the corresponding 1-D model (Stewart 2017).

In particular, the parameter space for $p_e = 2.2$ is shown in figure 10, illustrating the range of unstable Reynolds numbers for such upper branch oscillations, in this case between neutrally stable points N3 and N4. As noted in Wang *et al.* (2021*a*), the unstable range for the upper branch oscillations remains close to the transition line between upper and lower steady solutions (the estimated transition point is shown as an open pink square in figure 10(*a*), which lies between N3 and N4), while the system eventually stabilises as the Reynolds number decreases and the profile becomes more inflated (see steady profile at point N3, figure 10*a* inset); this gradual change is evident when comparing the steady wall profiles at N3, which is fully inflated, and N4, which is partially collapsed (see insets to figure 10*a*). However, stabilisation is not directly linked to the underlying steady profile becoming fully inflated (which occurs for $Re \approx 176.42$, well above the critical value for N3), but is instead linked to the unsteady dynamics of the oscillatory wall. For example, figure 10(*b*) shows the corresponding minimal channel width as a function of time, showing that the wall profile spends a smaller proportion of each period in a collapsed configuration (i.e. $y_{min}(t) < 1$) as the Reynolds number approaches N3. Furthermore, figure 10(*a*) suggests that the envelope of the global minimal channel width over a period (marked with red crosses in figure 10*a*) approaches exactly the width of the rigid segments as the Reynolds number reaches the critical value for N3. These observations suggest that
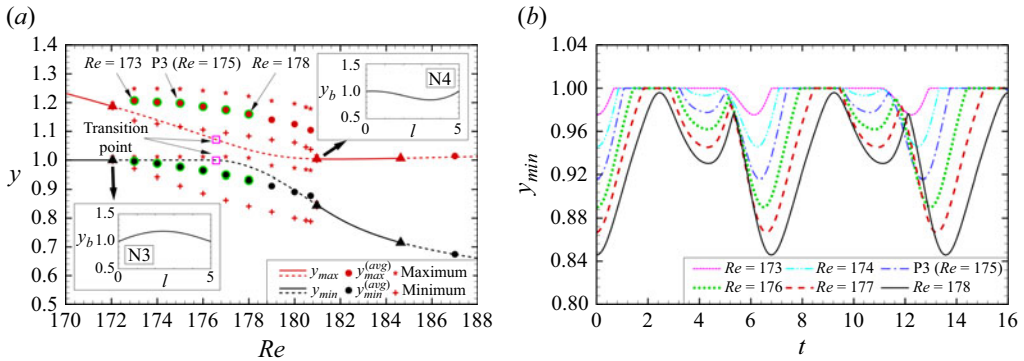
Figure 10. Steady and unsteady solutions of the 2-D model for $p_e = 2.2$, focusing on Reynolds numbers between neutral stability points N3 and N4: (*a*) maximal and minimal wall deflection as a function of Reynolds number from the steady model (black lines), time-averaged values computed from fully developed simulations of the unsteady model (filled circles) and corresponding global maximal/minimal values over a period (red crosses); (*b*) time trace of the minimal wall deflection from fully developed simulations of the unsteady model at $Re = 173$ (magenta), $Re = 174$ (cyan), $Re = 175$ (blue), $Re = 176$ (green), $Re = 177$ (red) and $Re = 178$ (black). The insets in (*a*) show the corresponding steady wall profiles at neutral stability points N3 and N4. The open green circles in (*a*) indicate Reynolds numbers considered in (*b*).

this oscillation growing from the upper branch is transitional, dependent on the wall profile being at least partially collapsed over a period.

In order to elucidate the corresponding mechanism of upper branch instability we again consider both the neutrally stable eigenfunctions (at operating point N3, figure 11) and fully nonlinear profiles of the saturated oscillatory limit cycle (operating point P3, figures 12 and 13). Although we focus primarily on the neighbourhood of N3 in the main text, note that movies for the upper branch oscillations at operating points P2, P3 and P4 are all available in the electronic supplementary material.

In order to examine the structure of a neutrally stable normal mode associated with these upper branch oscillations, figure 11 considers the dynamics of the 2-D system at neutral stability point N3. As discussed above, for this neutral stability point, the steady beam is fully inflated and almost perfectly symmetric about the centre of the compliant segment (figure 11*a*). The corresponding eigenfunction wall profile takes the form of a travelling wave propagating upstream against the mean flow (figure 11*b*), in contrast to the almost standing waves for the lower branch oscillations (see figure 5*b*). This upstream propagation is further evident when we trace the spatial location of the corresponding local minimum of the eigenfunction wall profile over a period (figure 11*c*), which gradually moves upstream over a period, eventually being replaced by a new minimum that develops at the downstream end of the compliant segment. The path traced is almost perfectly symmetric about the centre of the compliant segment (figure 11*c*), despite no apparent symmetries in the profiles themselves (figure 11*b*). Note that this upstream-propagating surface wave is almost exclusively a result of transverse motion of the wall material points (in the *y* direction) rather than longitudinal motion (in the *x* direction).

In order to investigate the corresponding fully developed (nonlinear) oscillations growing from the upper branch of steady solutions, in figure 12 we present a typical example at operating point P3 (a small increase in Reynolds number above neutral stability point N3), plotting the time trace of the mid-point wall pressure (figure 12*a*) and 10 equally spaced snapshots of the streamlines and pressure contours over a period (figure 12*b–k*). The dynamics is qualitatively similar to those described by Wang *et al.* (2021*a*) and so we focus only on the key points. Similar to the neutral stability eigenfunction (figure 11*b–e*),
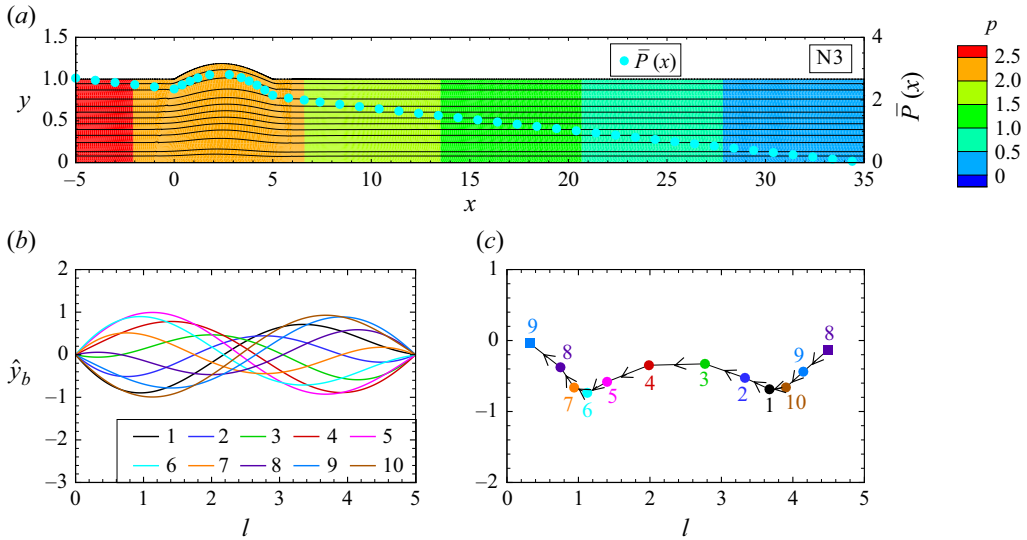
Figure 11. Neutrally stable self-excited oscillations originating from the upper branch of steady solutions for $p_e = 2.2$ as predicted by the 2-D model at point N3 ($Re = 172.05$): (*a*) steady flow-field and pressure contours, (*b*) eigenfunction wall profile plotted at 10 equally spaced snapshots over a period of oscillation, (*c*) spatial location and value of the local minimum of the perturbation wall profile over a period of oscillation. The eigenfunctions in (*b,c*) are normalised on the maximum of the modulus of the (complex-valued) wall profile. The cyan filled circles in (*a*) are the corresponding cross-stream averaged steady pressure distribution $\bar{P}(x)$.

a perturbation drives the wall inwards (outwards) at the upstream (downstream) end of the collapsible segment (figure 12*b*), gradually driving fluid downstream (figure 12*c*), further expanding the downstream end of the channel (figure 12*d*). This expanded region accumulates fluid and moves upstream, eventually collapsing the downstream end of the compliant segment (figure 12*e–g*). This accumulation continues to propagate upstream, before finally being suppressed through interaction with the upstream rigid segment (figure 12*h,i*), pushing the accumulation of fluid downstream again. This downstream motion subsequently inflates the downstream end of the compliant segment and collapses the upstream end (figure 12*j,k*) and the process repeats.

In order to explore the corresponding mechanism of the upper branch instability, figure 13 considers time traces of various quantities of interest including the upstream driving pressure (figure 13*a,b*), the difference in the cross-sectionally averaged streamwise pressure gradient compared with the steady value (figure 13*a,c*) and the spatially averaged wall deflection (figure 13*d*). Over a period of oscillation the upstream pressure is (on average) increased compared with the steady value (figure 13*a,b*), so in this case the oscillatory flow is working harder to sustain the instability (c.f. (2.10*c*)). The corresponding cross-sectionally averaged pressure gradient is increased slightly (less negative) compared with the steady configuration in the two rigid segments, while this quantity is much more strongly decreased in the compliant segment, again suggesting the flow is working harder than the corresponding steady configuration (figure 13*a,c*); such an increase in work done by the oscillating system is presumably due to the action of nonlinear Reynolds stresses, similar to other examples of self-excited oscillation in collapsible channels (e.g. Stewart *et al.* 2009; Wang *et al.* 2021*a*). In online supplementary material we further illustrate the corresponding spatial profiles of the flow components and the pressure at selected time points over an oscillation. In this case, these upper branch oscillations exhibit much greater pressure fluctuations in the transverse direction
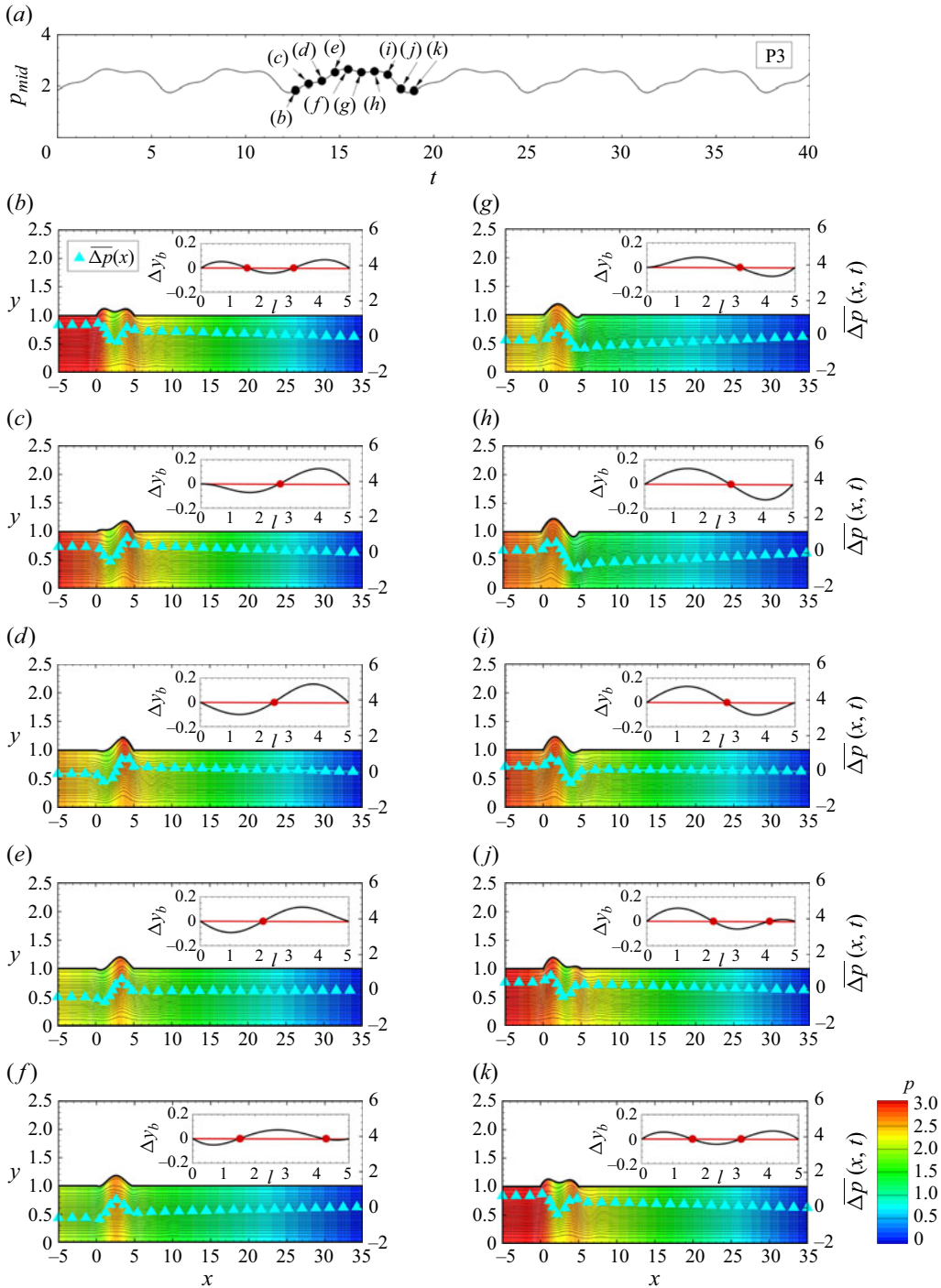
Figure 12. Fully developed self-excited oscillations growing from the upper branch of steady solutions predicted by the 2-D model at operating point P3 ($p_e = 2.2$, $Re = 175$): (a) time trace of the wall mid-point pressure p_{mid} over six periods of oscillation; (b–k) streamlines and pressure contours of the flow field at 10 equally spaced times over one period (times marked in panel a). The cyan filled triangles in (b–k) illustrate the excess (cross-stream averaged) instantaneous pressure compared with the steady pressure ($\overline{\Delta}p$). The insets in (b–k) show the difference between the instantaneous wall profile compared with the steady wall profile (Δy_b).
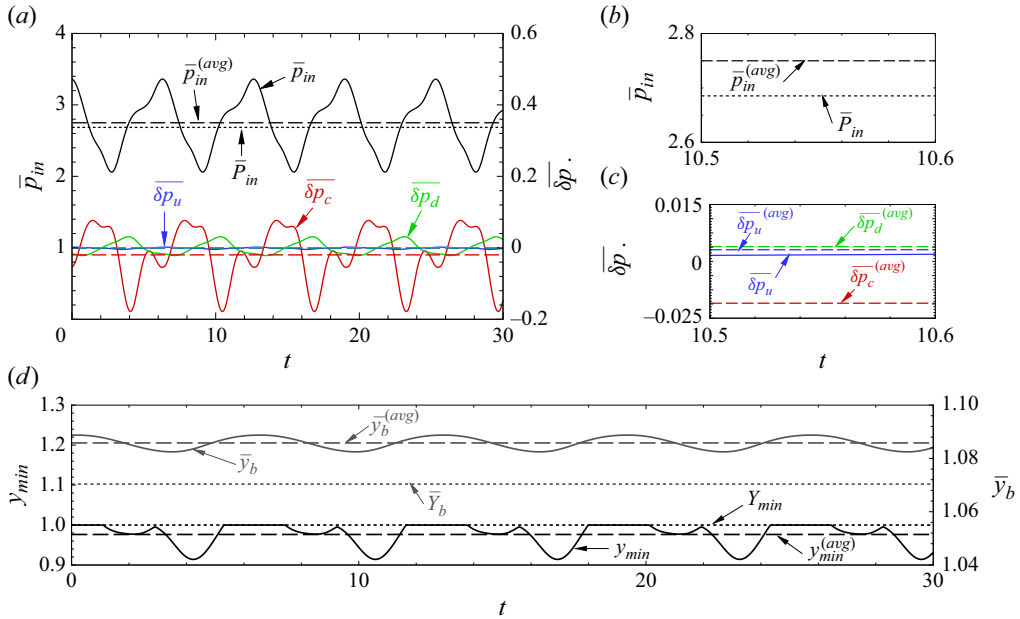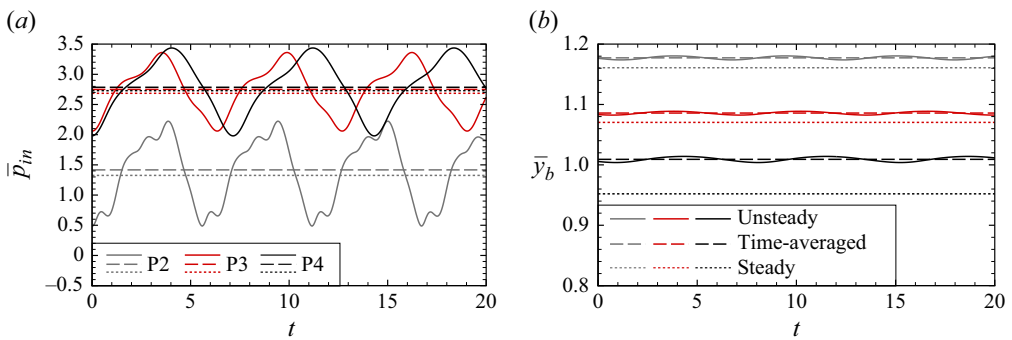
Figure 13. Fully developed self-excited oscillations growing from the upper branch of steady solutions at operating point P3 ($p_e = 2.2$, $Re = 175$), including (*a*) the time trace of the cross-sectionally averaged inlet pressure ($\overline{p}_{in}$, black curve) and the excess pressure gradient compared with the steady ($\delta p.$) in the upstream (blue curve), compliant (red curve) and downstream (green curve) segments; (*b*) a close-up of the time trace of the cross-sectionally averaged inlet pressure; (*c*) a close-up of the time trace of the excess pressure gradients in each segment; (*d*) the time trace of the minimal channel width (left axis) and the spatially averaged channel width (right axis). Note the corresponding time-averaged and steady values are denoted as dashed and dotted lines in panels (*a*–*d*).

Figure 14. Fully developed self-excited oscillations growing from the upper branch of steady solutions at operating points P2, P3 and P4: (*a*) time trace of the cross-sectionally averaged inlet pressure ($\overline{p}_{in}$), (*b*) time trace of the spatially averaged channel width ($\overline{y}_b$). The corresponding time-averaged and steady values are denoted as dashed and dotted lines.

compared with the lower branch oscillations and the streamwise component of the flow is increasingly non-parabolic. Hence, we conclude that the mechanism of these upper branch instabilities is very different to the lower branch, involving an increase in the rate of working of upstream pressure.

In order to check that our proposed mechanism for upper branch oscillation also applies more broadly across the parameter space, figure 14 compares time traces of the

upstream driving pressure (figure 14*a*) and the mean wall deflection (figure 14*b*) for upper branch oscillations at points P2, P3 and P4. Across all cases our observations are qualitatively similar, where the time-averaged upstream pressure again exceeds the steady value (figure 14*a*) and the wall is (on-average) more inflated than the steady profile (figure 14*b*).

7. Discussion

In this paper we have considered a prototypical model for fluid–structure interaction, involving flow through a finite-length flexible-walled channel at modest Reynolds numbers driven by a fixed upstream flow rate. The model is based on a formulation presented previously, where the flexible wall is modelled as a pre-tensioned nonlinear elastic beam, using an Arbitrary Lagrangian Eulerian method to handle the fluid–structure coupling combined with a finite element method (Luo *et al.* 2008; Wang *et al.* 2021*a*,*b*). We employed both fully nonlinear unsteady simulations of this model combined with a sophisticated linear stability eigensolver (Hao *et al.* 2016) to elucidate several families of self-excited oscillations that can grow from the underlying steady configurations of the system. We focused particularly on a parameter regime where the response of the elastic beam is dominated by the pre-tension, resembling earlier studies of flow in collapsible channels where the flexible wall was modelled as a pre-tensioned elastic membrane (Luo & Pedley 1996, 2000). This parameter regime also coincides with that used in simplified (semi-empirical) 1-D models of the same system (Xu *et al.* 2013, 2014; Stewart 2017), allowing the direct comparison of predictions.

In agreement with earlier studies, our computations indicate that the steady wall is inflated for low Reynolds numbers, gradually becoming more collapsed as the Reynolds number increases. In most cases studied this collapse is monotonic, and we delineate the transition between inflated (upper branch) states and collapsed (lower branch) states (figure 2). The system also exhibits a small region of parameter space with multiple coexisting steady states, but this is distinct from the neutral stability curves (figure 3).

The (collapsed) lower branch steady state becomes unstable to self-excited oscillations as the Reynolds number increases (figure 4), in close agreement with the predictions of a simplified 1-D model (Stewart 2017). For these oscillations, the corresponding neutrally stable eigenfunction is an almost perfect standing wave that is pinned close to the centre of the compliant segment, where the oscillating wall profile drives a corresponding flow within the compliant channel (figure 5). Furthermore, our computations have verified the mechanism of instability suggested by Stewart (2017), where on average (over a period) the fully developed oscillation results in a slight opening of the collapsed channel, resulting in less overall dissipation and so the upstream driving pressure is required to do less work, making an oscillation more favourable than the corresponding steady state (figure 7).

Moreover, numerical computations reproduced the family of high-frequency upper branch oscillations growing from the lower branch of steady solutions predicted by Stewart (2017), verifying that for these highly collapsed configurations the point of greatest channel collapse dictates the resulting structure of the eigenfunction wall profile (figure 8). However, the mechanism of instability is more difficult to decipher in this case as differences to the steady state are very small (figure 9).

In addition, our fully 2-D computations also exhibited two other families of self-excited oscillations growing from the upper branch of steady solutions; these modes were not predicted by the 1-D model of Stewart (2017). In particular, the computations predicted so-called 'upper branch' oscillations, which are unstable close to the transition between upper and lower branch steady states, stabilising when the channel becomes sufficiently inflated

so that the wall profile is no longer collapsed for any portion of a period of oscillation (figure 10). The nonlinear dynamics of these oscillations are very similar to our previous work in a different parameter regime (Wang *et al.* 2021*a*,*b*). However, the underlying mechanism of instability is now very different to oscillations growing from the lower branch of steady solutions, where the upstream pressure is (on average) increased over a period of oscillation, presumably as a result of the action of nonlinear Reynolds stresses (figure 13*a*,*b*), while the time-averaged pressure gradient along the compliant segment of the channel is decreased (i.e. more negative, figure 13*a*,*c*).

Finally, for much lower Reynolds numbers, the computational model also predicts a second family of self-excited oscillations growing from the upper branch of steady solutions, where the wall is now very highly inflated (figure 16). Although again these oscillations are driven by an overall increase in upstream pressure over a period, these so-called 'fully upper branch' oscillations exhibit only very small-amplitude perturbations to the beam profile, where the oscillatory flow is instead dominated by large-amplitude recirculation vortices evolving within the inflated cavity. These oscillations are qualitatively similar to upper branch oscillations reported by Herrada *et al.* (2022). Such oscillations growing from an inflated state are much less well studied than those from a collapsed state, but may help to explain self-excited oscillations observed in inflated blood vessels such as aortic aneurysms (Mast & Pierce 1995) or in the vortex vein ampullae of the choroid in the eye (Matsumoto *et al.* 2024). Investigations of such physiological applications are deferred to future work.

Appendix. Fully upper branch instability

In figure 3 we identified a new family of self-excited oscillations growing from the upper branch of steady solutions across a narrow range of external pressures. We termed these 'fully upper' branch oscillations, as the wall profile remains completely inflated across the entire period of oscillation, in contrast to the upper branch oscillations considered in § 6 where we showed that the wall spends a portion of each period in a partially collapsed state. In order to elucidate these fully upper branch oscillations, figure 15 considers neutral stability point N1, plotting both the steady configuration of the channel (figure 15*a*) alongside profiles of the neutrally stable eigenfunction wall profile (figure 15*b*). As expected given the relatively low value of the external pressure, the steady channel is significantly expanded along the compliant segment, with a large
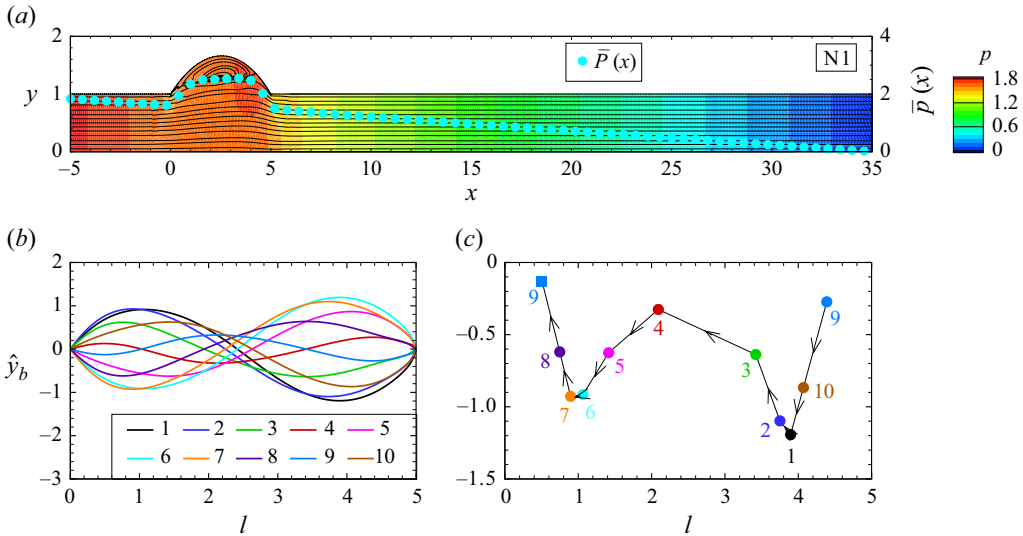
Figure 15. Neutrally stable self-excited oscillations originating from the upper branch of steady solutions for $p_e = 1$ as predicted by the 2-D model at point N1 ($Re = 250.01$): (*a*) steady flow-field and pressure contours, (*b*) eigenfunction wall profile plotted at 10 equally spaced snapshots over a period of oscillation, (*c*) spatial location and value of the local minimum of the perturbation wall profile over a period of oscillation. The eigenfunctions in (*b,c*) are normalised on the maximum of the modulus of the (complex-valued) wall profile. The cyan filled circles in (*a*) indicate the corresponding steady cross-stream averaged pressure distribution.

recirculation vortex within the inflated cavity (figure 15*a*); the corresponding fluid pressure is almost uniform across the cavity, comparable to the inlet driving pressure and the eigenfunction wall profiles are all mode-2 (figure 15*b*). Similar to the upper branch oscillations discussed in § 6, the perturbation wall motion takes the form of an upstream propagating travelling wave, where we observe gradual upstream motion of the point of maximal constriction (figure 15*c*); upstream propagation eventually terminates as the wave is suppressed (rather than reflected) by the upstream rigid segment and is replaced by a new minimum that develops at the downstream end of the compliant segment and propagates upstream. In summary, this figure demonstrates that although the steady flow profiles are substantially different between the fully upper branch and upper branch oscillations, the corresponding perturbation eigenfunctions share many of the key features including an upstream-propagating travelling wave.

In order to elucidate this new family of fully upper oscillations, figure 16 illustrates the nonlinear dynamics of a typical example that has saturated into its nonlinear limit cycle (operating point P1), showing time traces of the cross-sectionally averaged upstream pressure (figure 16*a,b*), the corresponding difference in the (spatially) averaged pressure gradient between the steady and unsteady flows in each segment (figure 16*a,c*), the spatially averaged beam deflection (figure 16*d*) and 10 equally spaced snapshots of the streamlines and pressure contours over a period (figure 16*e–n*). As expected, given the shape of the underlying steady configuration, the wall profile remains highly inflated over the entire period of oscillation while deflections to the wall profile are very small (compared with the large steady deflection); the difference between the wall profile and the corresponding steady configuration is shown as an inset in figure 16(*e–n*), where the maximal amplitude is up to 3.53 % of the channel width (figure 16*g*), compared with a maximal amplitude of at most 15.0 % of the channel width for upper branch oscillations at operating point P3 (figure 12*d*). Similarly, the range of variation in the upstream pressure (and the spatially averaged pressure gradients) are much smaller: at operating point P6 the ratio between the
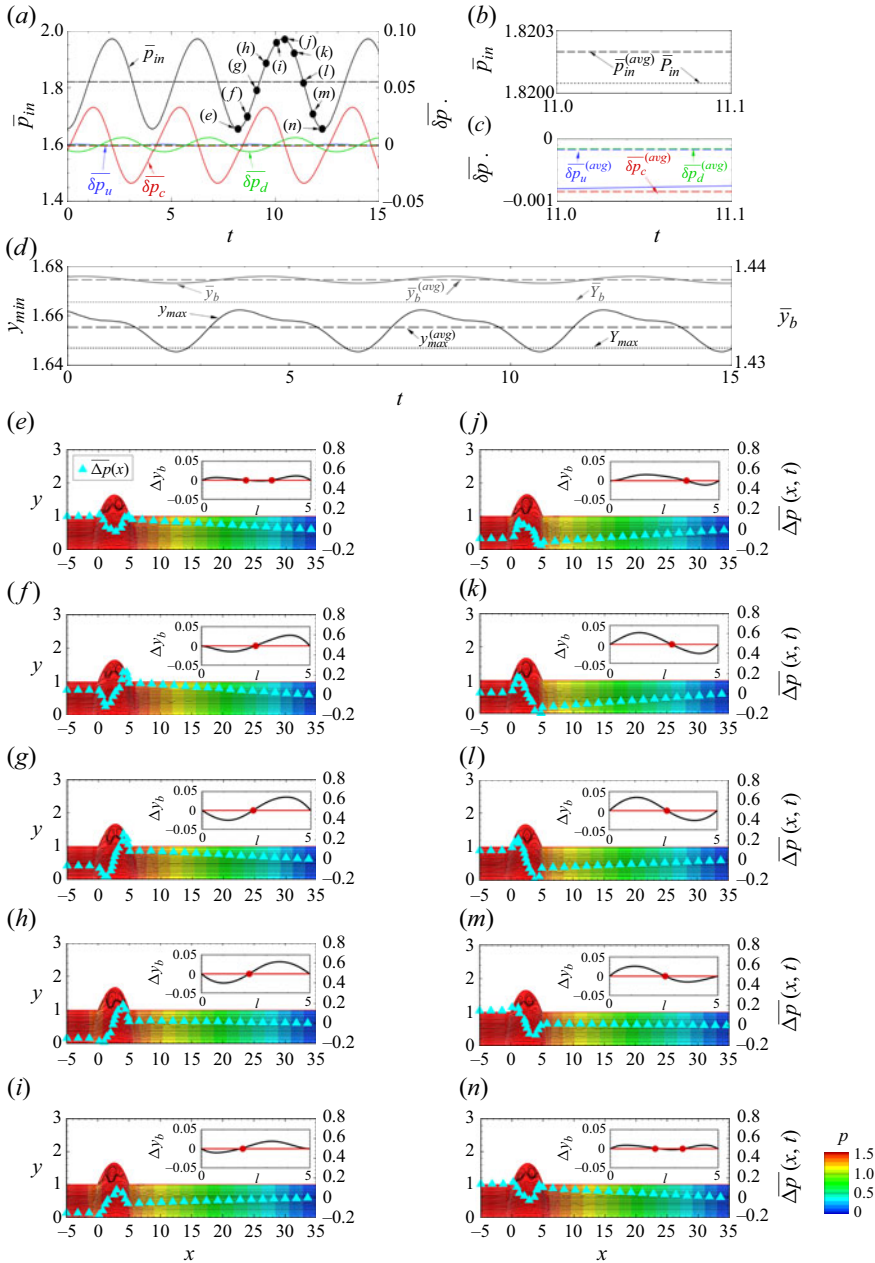
Figure 16. Fully developed self-excited oscillations growing from the upper branch of steady solutions predicted by the 2-D model at operating point P1 ($p_e = 1$, $Re = 253$): (*a*) time trace of the cross-sectionally averaged inlet pressure ($\bar{p}_{in}$, black curve) and the excess pressure gradient compared with the steady (δp.) in the upstream (blue curve), compliant (red curve) and downstream (green curve) segments; (*b*) close-up of the time trace of the cross-sectionally averaged inlet pressure; (*c*) close-up of the time trace of the excess pressure gradients in each segment; (*d*) time trace of the minimal channel width (left axis) and the spatially averaged channel width (right axis); (*e–n*) streamlines and pressure contours of the instantaneous flow field at 10 equally spaced time instances over one period (times marked in panel *a*). The cyan filled triangles in (*e–n*) illustrate the excess between the (cross-stream averaged) instantaneous pressure compared with the steady pressure ($\overline{\Delta}p$). The insets in (*e–n*) show the difference between the instantaneous wall profile compared with the steady wall profile (Δy_b).

excess upstream pressure compared with the steady value is just 0.008 % (figure 16*a*,*b*) compared with 2.4 % at operating point P3 (figure 13*a*,*b*).

One striking feature is the presence of large recirculation vortices within the inflated portion of the channel, evident in both the steady configuration (figure 15*a*) and the unsteady snapshots (figure 16*e–n*). Such recirculation is not unexpected given the large cavity formed by the wall deflection: the flow beneath the inflated region remains almost entirely laminar and unidirectional (consistent with the unidirectional flow in the adjacent rigid segments), but drive a large-scale rotational flow within the inflated segment, reminiscent of a lid-driven cavity (e.g. Kuhlmann & Romanò 2019; Shankar & Deshpande 2000) and flow in a rigid channel with wavy walls (e.g. Cho, Kim & Shin 1998). The unsteady wall profiles exhibit a small-amplitude perturbation superimposed on the steady configuration (see the wall deflection profiles shown as insets in figure 16*e–n*); this perturbation arises as an inflated hump that grows from the downstream end of the compliant segment (see figure 16*e*,*f*) and then gradually propagates upstream (figure 16*g–i*). Conservation of mass means that the wall eventually deflects inwards (compared with the steady profile) at the downstream end of the compliant segment as its bulges toward the upstream end (figure 16*j–l*). Consistent with the predictions of the linear stability eigensolver, eventually the upstream propagation of the outward bulge is suppressed by interaction with the upstream rigid segment (figure 16*m*), at which point another inflated hump appears at the downstream end of the compliant segment (see figure 16*n*) and the process repeats. However, despite the strong similarities in appearance, this new branch of self-excited oscillations growing from the upper branch of steady solutions is only evident when the steady configuration is highly inflated, contrary to the oscillations discussed in § 6 that remain localised to the transition region between upper and lower steady configurations. In this regard, our new fully upper self-excited oscillations are more similar to those discussed by Herrada *et al.* (2022), where again the channel wall is much more inflated on average and recirculation is a striking feature of the flow. Such recirculation could not be predicted by the 1-D model (2.16), suggestive as to why this family of oscillations is not predicted there.

In each snapshot the corresponding (cross-sectionally averaged) pressure gradient remains constant (essentially zero) across the upstream rigid segment and almost perfectly linear in the downstream rigid segment, while there are large-scale pressure variations across the compliant segment (figure 16*e–n*). Such variations are also evident in the difference between the (cross-sectionally averaged) pressure gradient across each segment compared with the steady state (figure 16*a*,*c*). Similarly, the time-averaged driving pressure is again increased compared with the corresponding steady flow, suggesting that the rate of working of upstream pressure (c.f. (2.10*c*)) is increased in the oscillatory state (figure 16*a*,*b*). Furthermore, the spatially averaged beam deflection and the maximal beam deflections are both increased over a period compared with their corresponding steady values (figure 16*d*). Further snapshots of the flow profile over a period of oscillation are shown in online supplementary material, which we again note that the deviations from the underlying steady flow exhibit very small amplitudes.

REFERENCES

ARMITSTEAD, J.P., BERTRAM, C.D. & JENSEN, O.E. 1996 A study of the bifurcation behaviour of a model of flow through a collapsible tube. *Bull. Math. Biol.* **58**, 611–641.

BERTRAM, C.D. & PEDLEY, T.J. 1982 A mathematical model of unsteady collapsible tube behaviour. *J. Biomech.* **15** (1), 39–50.

BERTRAM, C.D., RAYMOND, C.J. & PEDLEY, T.J. 1990 Mapping of instabilities for flow through collapsed tubes of differing length. *J. Fluids Struct.* **4** (2), 125–153.

BERTRAM, C.D., RAYMOND, C.J. & PEDLEY, T.J. 1991 Application of nonlinear dynamics concepts to the analysis of self-excited oscillations of a collapsible tube conveying a fluid. *J. Fluids Struct.* **5** (4), 391–426.

CAI, Z.X. & LUO, X.Y. 2003 A fluid–beam model for flow in a collapsible channel. *J. Fluids Struct.* **17** (1), 125–146.

CHO, K.J., KIM, M.U. & SHIN, H.D. 1998 Linear stability of two-dimensional steady flow in wavy-walled channels. *Fluid Dyn. Res.* **23** (6), 349.

CHOWDHURY, S.K. & ZHANG, Y. 2024 An experimental study of fluid–structure interaction and self-excited oscillation in thin-walled collapsible tube. *Phys. Fluids* **36** (7), 071902.

DRAZIN, P.G. 2002 *Introduction to Hydrodynamic Stability*. Cambridge University Press.

GROTBERG, J.B. 2021 *Biofluid Mechanics*. Cambridge University Press.

HAO, Y.J., CAI, Z.X., ROPER, S. & LUO, X.Y. 2016 An Arnoldi-frontal approach for the stability analysis of flows in a collapsible channel. *Int. J. Appl. Mech.* **8** (06), 1650073.

HAZEL, A.L. & HEIL, M. 2003 Steady finite-Reynolds-number flows in three-dimensional collapsible tubes. *J. Fluid Mech.* **486**, 79–103.

HEIL, M. 2004 An efficient solver for the fully coupled solution of large-displacement fluid–structure interaction problems. *Comput. Methods Appl. Mech. Eng.* **193** (1–2), 1–23.

HEIL, M. & BOYLE, J. 2010 Self-excited oscillations in three-dimensional collapsible tubes: simulating their onset and large-amplitude oscillations. *J. Fluid Mech.* **652**, 405.

HEIL, M. & HAZEL, A.L. 2011 Fluid-structure interaction in internal physiological flows. *Annu. Rev. Fluid Mech.* **43**, 141–162.

HERRADA, M.A., BLANCO-TREJO, S., EGGERS, J. & STEWART, P.S. 2022 Global stability analysis of flexible channel flow with a hyperelastic wall. *J. Fluid Mech.* **934**, A28.

HUANG, L. 2001 Viscous flutter of a finite elastic membrane in Poiseuille flow. *J. Fluids Struct.* **15** (7), 1061–1088.

HUANG, Q., TIAN, F.-B., YOUNG, J. & LAI, J.C.S. 2021 Transition to chaos in a two-sided collapsible channel flow. *J. Fluid Mech.* **926**, A15.

HUANG, Q.X., LIU, Z.L., WANG, L., RAVI, S., YOUNG, J., LAI, J.C.S. & TIAN, F.B. 2022 Streamline penetration, velocity error, and consequences of the feedback immersed boundary method. *Phys. Fluids* **34** (9), 097101.

IKEDA, T., HEIL, M., BEAUGENDRE, H. & PEDLEY, T.J. 1998 Experiments on flow in a two-dimensional collapsible channel. In *Third World Congress of Biomechanics, Abstracts, Sapporo, Japan*, p. 38b.

JENSEN, O.E. 1990 Instabilities of flow in a collapsed tube. *J. Fluid Mech.* **220**, 623–659.

JENSEN, O.E. & HEIL, M. 2003 High-frequency self-excited oscillations in a collapsible-channel flow. *J. Fluid Mech.* **481**, 235–268.

KUHLMANN, H.C. & ROMANÒ, F. 2019 The lid-driven cavity. In *Computational Modelling of Bifurcations and Instabilities in Fluid Dynamics* (ed. A. GELFGAT), pp. 233–309. Springer International Publishing.

LIU, H.F., LUO, X.Y. & CAI, Z.X. 2012 Stability and energy budget of pressure-driven collapsible channel flows. *J. Fluid Mech.* **705**, 348–370.

LUO, X.Y., CAI, Z.X., LI, W.G. & PEDLEY, T.J. 2008 The cascade structure of linear instability in collapsible channel flows. *J. Fluid Mech.* **600**, 45–76.

LUO, X.Y. & PEDLEY, T.J. 1996 A numerical simulation of unsteady flow in a two-dimensional collapsible channel. *J. Fluid Mech.* **314**, 191–225.

LUO, X.Y. & PEDLEY, T.J. 1998 The effects of wall inertia on flow in a two-dimensional collapsible channel. *J. Fluid Mech.* **363**, 253–280.

LUO, X.Y. & PEDLEY, T.J. 2000 Multiple solutions and flow limitation in collapsible channel flows. *J. Fluid Mech.* **420**, 301–324.

MARZO, A., LUO, X.Y. & BERTRAM, C.D. 2005 Three-dimensional collapse and steady flow in thick-walled flexible tubes. *J. Fluids Struct.* **20** (6), 817–835.

MAST, T.D. & PIERCE, A.D. 1995 A theory of aneurysm sounds. *J. Biomech.* **28** (9), 1045–1053.

MATSUMOTO, H., KISHI, S., HOSHINO, J., NAKAMURA, K. & AKIYAMA, H. 2024 Inversion of asymmetric vortex vein dilatation in pachychoroid spectrum diseases. *Ophthalmol. Sci.* **4** (5), 100515.

PAIDOUSSIS, M.P. 2013 *Fluid-Structure Interactions, Slender Structures and Axial Flow*. Elsevier.

PEDLEY, T.J. 1992 Longitudinal tension variation in collapsible channels: a new mechanism for the breakdown of steady flow. *J. Biomech. Eng.* **114** (1), 60–67.

RILEY, J.J., GAD-EL HAK, M. & METCALFE, R.W. 1988 Complaint coatings. *Ann. Rev. Fluid Mech.* **20** (1), 393–420.

SHANKAR, P.N. & DESHPANDE, M. 2000 Fluid mechanics in the driven cavity. *Ann. Rev. Fluid. Mech.* **32** (1), 93–136.

STEWART, P.S. 2010 Flows in flexible channels and airways. *PhD thesis*, University of Nottingham.

STEWART, P.S. 2017 Instabilities in flexible channel flow with large external pressure. *J. Fluid Mech.* **825**, 922–960.

STEWART, P.S., HEIL, M., WATERS, S.L. & JENSEN, O.E. 2010 Sloshing and slamming oscillations in a collapsible channel flow. *J. Fluid Mech.* **662**, 288–319.

STEWART, P.S., WATERS, S.L. & JENSEN, O.E. 2009 Local and global instabilities of flow in a flexible-walled channel. *Eur. J. Mech. B/Fluids* **28** (4), 541–557.

TANG, C., ZHU, L.D., AKINGBA, G. & LU, X.Y. 2015 Viscous flow past a collapsible channel as a model for self-excited oscillation of blood vessels. *J. Biomech.* **48** (10), 1922–1929.

VERMA, M.K.S. & KUMARAN, V. 2012 A dynamical instability due to fluid–wall coupling lowers the transition Reynolds number in the flow through a flexible tube. *J. Fluid Mech.* **705**, 322–347.

VERMA, M.K.S. & KUMARAN, V. 2013 A multifold reduction in the transition Reynolds number, and ultra-fast mixing, in a micro-channel due to a dynamical instability induced by a soft wall. *J. Fluid Mech.* **727**, 407–455.

WANG, D.Y. 2019 The energetics of self-excited oscillations in collapsible channel flows, *PhD thesis*. University of Glasgow.

WANG, D.Y., LUO, X.Y. & STEWART, P.S. 2021*a* Energetics of collapsible channel flow with a nonlinear fluid-beam model. *J. Fluid Mech.* **926**, A2.

WANG, D.Y., LUO, X.Y. & STEWART, P.S. 2021*b* Multiple steady and oscillatory solutions in a collapsible channel flow. *Int. J. Appl. Mech.* **13** (06), 2150058.

WANG, X. & CHRISTOV, I.C. 2022 Reduced modelling and global instability of finite-Reynolds-number flow in compliant rectangular channels. *J. Fluid Mech.* **950**, A26.

WHITTAKER, R.J. 2015 A shear-relaxation boundary layer near the pinned ends of a buckled elastic-walled tube. *IMA J. Appl. Math.* **80** (6), 1932–1967.

WHITTAKER, R.J., WATERS, S.L., JENSEN, O.E., BOYLE, J. & HEIL, M. 2010 The energetics of flow through a rapidly oscillating tube. Part 1. General Theory. *J. Fluid Mech.* **648**, 83–121.

XU, F., BILLINGHAM, J. & JENSEN, O.E. 2013 Divergence-driven oscillations in a flexible-channel flow with fixed upstream flux. *J. Fluid Mech.* **723**, 706–733.

XU, F., BILLINGHAM, J. & JENSEN, O.E. 2014 Resonance-driven oscillations in a flexible-channel flow with fixed upstream flux and a long downstream rigid segment. *J. Fluid Mech.* **746**, 368–404.

XU, F. & JENSEN, O.E. 2015 A low-order model for slamming in a flexible-channel flow. *Q. J. Mech. Appl. Math.* **68** (3), 299–319.

ZHANG, S., LUO, X.Y. & CAI, Z.X. 2018 Three-dimensional flows in a hyperelastic vessel under external pressure. *Biomech. Model. Mechanobiol.* **17**, 1187–1207.